VALIDATION OF RADIOCARPAL JOINT CONTACT MODELS BASED ON IMAGES FROM A CLINICAL MRI SCANNER

BY

Joshua Eddie Johnson

Submitted to the graduate degree program in Mechanical Engineering
and the Graduate Faculty of the University of Kansas
in partial fulfillment of the requirements for the degree of
Master of Science in Mechanical Engineering

_____
Chairperson

Committee members _____

_____

_____

Date defended: _____

The Thesis Committee for Joshua Eddie Johnson certifies
that this is the approved Version of the following thesis:

VALIDATION OF RADIOCARPAL JOINT CONTACT MODELS BASED ON IMAGES FROM A CLINICAL MRI SCANNER

Committee:

_____
Chairperson

_____

_____

_____

Date approved: _____

Acknowledgement

The fear of the LORD is the beginning of wisdom,

and knowledge of the Holy One is understanding.

Proverbs 9:10 (NIV)

First and foremost, I would like to thank my Lord and Savior Jesus Christ for the gift of life and the opportunity and privilege to pursue academic excellence. With Him, all things are possible. I would like to thank my advisor Dr. K. J. Fischer for picking me as his graduate student and providing all the necessary resources to bring this to pass. I thank him for all his input and assistance in ensuring that this project remained on track. I thank my committee members Drs. E. A. Friis and C. W. Luchies for all their invaluable help and support throughout the duration of my studies. I extend my gratitude to all the Department of Mechanical Engineering faculty, staff and colleagues who have contributed in some part or another in this venture. I sincerely thank the Hoglund Brain Imaging Center and the Orthopedic Research Center at the University of Kansas Medical Center for their assistance and the use of their facilities vital for the completion of this project. I should not forget undergraduate research assistant B. Hatesoh for his valuable help around the lab. Last but not the least; I would like to deeply thank my family and friends for their continued prayers and moral support without which things would have definitely been more cumbersome.

Abstract

Due to the severity and continuing escalation in occurrences of degenerative joint diseases, it is vital to establish a means of detection and prevention that could lead to an improvement in quality of life. One such means is MRI-based modeling for joint contact analysis of *in vivo* functional loading. The purpose of this study was to validate models generated from a clinical MR scanner for future *in vivo* joint contact analyses. Models were tested using 3 cadaver forearm specimens and compared with experimental data. It was found that models were validated based on contact area. Direct contact area measurements were observed to be very close to experimental data. Model force measurements were reasonable, but did not agree with experimental data as well as contact area. Peak pressure data from the models were less consistent in correspondence with experimental data. Also, radiocarpal mechanics were investigated to determine the effect of inserting a sensor into the joint space. Magnitudes of bone motions were found to be greater with film inserted than without film. Model results showed contact areas to be higher with film than without film.

Table of Contents

Table of Figures

Motivation and Research Objectives

Degeneration of articular surfaces leading to joint dysfunction is known as arthritis and it is currently the most prevalent of the joint diseases. Osteoarthritis (OA) is the most common form of arthritis and affects people all over the world and more often than not, leads to long term disability. OA is also known as degenerative joint disease, which is a progressive loss of articular cartilage, accompanied by attempted repair, remodeling and sclerosis of subchondral bone and osteophyte formation. Early signs include chronic joint pain eventually resulting in loss of motion. This leads to the inability to perform day-to-day activities and loss in quality of life and has a major impact on the economy. OA of the hand and wrist is second only to the knee in terms of incidence and therefore poses an important clinical problem. Finding a means of prevention before occurrence, would go a long way in improving quality of life for many.

The pathomechanics of OA is relatively unknown. One of the factors resulting in joint degeneration leading to primary OA is believed to be excessive articular surface contact stresses. On the other hand, secondary OA occurs mainly as a result of progressive joint degeneration caused by injuries (such as scapholunate dissociation). MRI-based modeling can help to predict OA risk. This method has been identified as a valuable tool for *in vivo* joint contact analyses. It is a non-invasive means of evaluating contact characteristics from imaging data during functional loading. Contact mechanics such as forces, areas and pressure distributions can be determined using this technique.

The availability of *in vivo* contact mechanics data (especially contact pressures) may help determine the relationship between joint loading and OA. Contact patterns and

intensities of healthy subjects can be monitored using models over a period of time to observe for changes in kinematics or contact mechanics that might lead to joint degeneration. If abnormality is observed, appropriate corrections can be implemented to restore normal contact behavior and prevent occurrence of degenerative joint diseases (DJD).

In vivo contact mechanics data can provide a means to determine efficacy of surgical procedures (such as proximal row carpectomy and scapholunate ligament repair) used to treat joint injuries which might progressively lead to OA. Contact patterns can be compared before and after surgical reconstruction procedures to treat joint injuries. Longitudinal studies of injured human subjects, observed for a period of time to monitor for progressive joint degeneration, may identify key factors leading to DJD/ OA.

Primary Objective

The purpose of this study was to validate models generated from a clinical MR scanner for future *in vivo* joint contact analysis. Validation of models would allow progression to the next phase, which is *in vivo* testing.

Secondary Objective

This study also aimed to determine the effects of inserting a pressure sensor into the joint space on radiocarpal kinematics and subsequent contact characteristics. The hypothesis was that contact areas and peak contact pressures obtained from models would be higher with the presence of sensor.

1. Introduction

The human hand has been a topic of universal interest for quite a period of time and amongst the most widely studied, except perhaps the brain. The hand has been characterized as a symbol of power [1], as an extension of intellect [2], and as the seat of the will [3]. While the brain is responsible for the design of civilization, the hand is responsible for its formation. The entire upper limb is subservient to the hand and the intricate mechanisms and functions thereof, have led to the detailed study of the finely balanced complexities of the upper extremity.

1.1. Anatomy

The hand is connected to the forearm by a collection of bones and soft tissue structures known as the wrist or carpus. The wrist joint complex with its arc of motion appears to be the key to hand function. It plays a vital role in positioning the hand in space while wrist stability and position affects finger flexion-extension and grasp. Kinematically, the wrist caters for relative motion between the hand and forearm while kinetically, transmits loads from the hand to the forearm and vice versa.

1.1.1. Bones of the Forearm

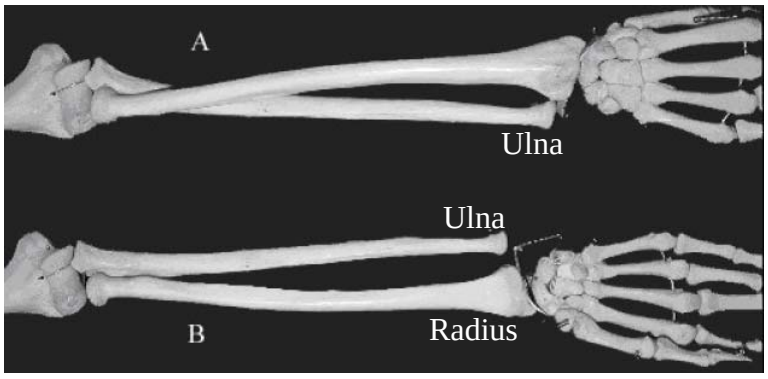

Figure 1.1 Forearm in pronation (A) and supination (B).

The section of the upper extremity from the distal elbow to the proximal wrist is known as the forearm (Fig. 1.1). The radius and ulna comprise the bones of the forearm, which are in contact with each other at the both the proximal and distal ends. Proximal articular complex is known as the proximal radioulnar joint and similarly the distal articulation, ligaments and cartilage complex make up the distal radioulnar joint [4]. The annular ligament, interosseous membrane, and the distal radioulnar ligaments stabilize these joints and allow radius rotation about the ulna [5].

The motions of the forearm are pronation and supination and these play a vital role in hand and wrist function. At 90° elbow flexion, superior orientation of the dorsum of the hand is referred to as pronation while superior orientation of the palm is referred to as supination. Average range of pronation-supination motion is 150° (60-80° of pronation and 60-85° of supination). The radius rotates across the ulna in pronation, and bears approximately 80% of the axial load at the wrist [6]. Some studies indicate that the ulna's load bearing increases proximally and may bear the majority of the load [7,8]. At the proximal end, the forearm bones are in articulation with the distal humerus of the upper arm, while at the distal end, they are in articulation with the proximal carpal bones of the wrist.

1.1.2. Bones of the Wrist

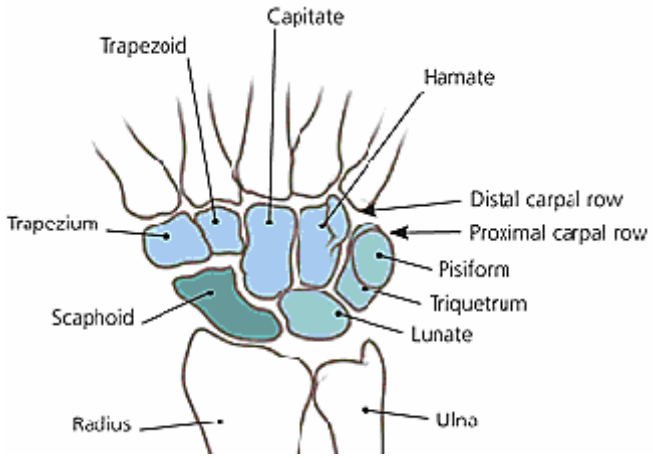

Figure 1.2 Wrist anatomy – dorsal view (public domain).

Even though we speak of the wrist as a joint, it is in fact a composite articulation of multiple bones (Fig. 1.2). Overall motion is a result of interaction amongst the carpal bones themselves and proximally and distally with the distal forearm bone articulation (triangular fibrocartilage complex) and metacarpals respectively [9].

There exist eight carpal bones that are anatomically divided into the proximal and distal carpal rows. From radial to ulnar, the scaphoid, lunate, triquetrum and pisiform constitute the proximal carpal row while the trapezium, trapezoid, capitate and hamate constitute the distal row. Even though the pisiform is considered as a proximal carpal row bone, it is a sesamoid within the flexor carpi ulnaris tendon. The scaphoid spans the midcarpal joint and acts as a mechanical link between the proximal and distal carpal rows [10].

1.1.3. The Wrist Complex

The radiocarpal and midcarpal joints together make up the wrist complex. The function of the wrist complex pertains more towards balance and control in positioning the hand in space which cannot be compensated either by shoulder, elbow or forearm [11]. Hence, from an anatomic and physiologic perspective, the wrist has been labeled as the most intricate joint of the body [12]. The structure and biomechanics of the wrist differ amongst individuals but as a whole, it is considered to be biaxial with flexion/extension about the medial-lateral axis and abduction/adduction about the anteroposterior axis.

This study focuses on the radiocarpal joint. The radius and radioulnar disk (part of the triangular fibrocartilage complex TFCC) make up the proximal section while the triquetrum, lunate and scaphoid make up the distal section. The proximal section has a biconcave surface and is divided into three facets. The scaphoid and radius articulate in the lateral facet, the lunate and radius in the medial facet and the TFCC articulates mainly with the triquetrum though it has partial contact with the lunate in neutral position. The TFCC functions as an extension of the distal radius and is partially attached to the ulna, which otherwise does not contribute to the radiocarpal joint.

1.1.4. Ligaments and Musculature

Ligaments of the wrist can be divided into two main categories; intrinsic and extrinsic. Intrinsic ligaments interconnect the carpal bones while the extrinsic ligaments connect the carpal bones to radius and ulna proximally or to metacarpals

distally. The main ligaments of the radiocarpal joint are the volar radiocarpal ligament, the radial and ulnar collateral ligaments and the scapholunate interosseous ligament. These function to provide joint stability while allowing necessary freedom of motion.

Wrist flexion/extension and radioulnar deviation are complex motions and require appropriate muscle-tendon groups to transmit forces to the bones. These function to provide a stable base while allowing positional adjustments. The primary wrist flexors are the palmaris longus, flexor carpi radialis and flexor carpi ulnaris while the primary extensors are the extensor carpi radialis longus and brevis and extensor carpi ulnaris. There exist other secondary wrist flexors and extensors that aid in function.

1.2. Pathologies of the Wrist Joint

Based on anatomy, it is observed that the wrist is a complex joint comprising of multiple bones and articulations, and as such it is prone to various injuries and pathologies. These injuries and pathologies can be a result of abnormal loading, joint instability and wear and tear. Some of the consequences of fracture, disease and arthritis are discussed below.

1.2.1. Fracture

Of all fractures and dislocations in the body, 6% occur at the wrist, the bones of the proximal row being the most common site of debilitating injury [13]. Colles fracture, which is the most common type of wrist fracture, occurs at the distal radius [14] while the scaphoid is the most frequently fractured of the carpal bones.

Colles fracture occurs frequently in adults, particularly middle-aged and elderly women, who exhibit osteoporosis and has a high rate of malunion. Improper healing can result in shortening or misalignment of the distal radius, with damage to the median nerve that may ultimately lead to carpal tunnel syndrome.

About 70% of carpal bone fractures occur at the scaphoid, and this fracture is most prominent in men between 15 and 30 years [15]. Maximum strain of the scaphoid was found at neutral radial/ulnar deviation and wrist extension [16], which is the position of the outstretched hand breaking a fall. This is a common case in sporting injuries and riding accidents such as bicycles and motorcycles. Depending on the angle of impact, it is either the distal radius or the scaphoid that is likely to fracture. A scaphoid fracture can occur with little or no deformity, limited soft tissue inflammation, and more often than not, without clear indication of a break. Non-union or necrosis can occur due to disruption in blood supply to the distal scaphoid as a result of fractures mostly happening in mid-proximal region. The scaphoid is also involved in the most common carpal instability syndrome known as scapholunate instability or radial perilunate instability.

1.2.2. Kienbock's Disease

Overloading of the lunate can lead to a disruption in blood supply resulting in a disorder known as Kienbock's disease [17]. This is characterized by a progressive loss in bone density, with no changes in geometry during the initial stages leading to lunate necrosis and eventually arthritis of the adjacent bones. MRI is the most common form of diagnosis used to identify symptoms especially at an early stage.

Depending on the severity of lunate/wrist damage, Iwasaki classifies Kienbock's disease into four categories/stages [18]. Stage I is the acute stage, during which the disease is hard to differentiate from a wrist sprain, and symptoms may subside after several weeks. Stage II includes changes in lunate bone density. During this stage lunate geometry remains intact, accompanied by joint pain and inflammation. Decreased mobility in the wrist joint is typical of Stage III, with the lunate beginning to collapse and migration of other carpal bones (the capitate in particular). Finally during Stage IV, the lunate disintegrates leading to wrist arthritis.

1.2.3. Preiser's Disease

This disease is characterized by spontaneous necrosis of the scaphoid and is not a common pathology of the wrist joint. Cystic and sclerotic changes precede total collapse of the bone. Preiser's disease may occur due to trauma, repetitive stress, or fatigue of the scaphoid. Radiographic features of the scaphoid are similar to that of the lunate affected by Kienbock's disease.

As with Kienbock's disease, Preiser's disease progresses in four stages. Stage I includes early changes in the scaphoid, and MRI of the wrist is abnormal. During Stage II, geometry of the bone is preserved, but contrasts are evident between the distal and proximal poles. Stage III is characterized by deformation of the scaphoid geometry, often with fragmentation. Stage IV heralds the collapse of the scaphoid, and arthritis of the radioscaphoid joint.

1.2.4. Osteoarthritis

Degeneration of articular surfaces leading to joint dysfunction is known as arthritis and it is currently the most prevalent of the joint diseases. About 21% of the adult population in the United States is affected by arthritis [National Center for Health Statistics, 2002] and 25% of the population over the age of 55 report incidence in some form [19].

Osteoarthritis (OA) is the most common form of arthritis and affects people all over the world, irrespective of nation, tribe, or tongue. In most populations over the age of 65, it is the most common cause of long-term disability especially in women. More than 20 million Americans are estimated to suffer from OA. World Health Organization estimates 10% of the world's population over 60 to suffer from OA of which 80% endure limited range of motion and 25%, the inability to perform day-to-day activities [20]. OA is impartial and can affect any synovial joint, the common ones being the knee, hip and wrist.

OA is synonymous with joint degeneration, which is a progressive loss of articular cartilage, accompanied by attempted repair, remodeling and sclerosis of subchondral bone and osteophyte formation. In fact, OA is often called degenerative joint disease (DJD). Early signs include chronic joint pain (deep aching poorly localized discomfort) leading to restriction in joint motion. Further degeneration results in loss of motion, crepitus, grating/grinding sensation and joint enlargement due to osteophyte formation. Joint subluxation, deformity, malalignment and muscle atrophy develop with advanced disease [20].

OA is classified into primary and secondary OA, primary being the more common of the two. The cause of joint degeneration leading to primary OA is relatively unknown and is believed to be a combination of age, excessive articular surface contact stresses and deterioration of chondrocyte function. Primary OA rarely occurs in people under the age of 40. On the other hand, secondary OA occurs as a result of joint degeneration caused by injuries or a variety of hereditary, inflammatory or developmental, metabolic and neurologic disorders and may affect younger adults [20].

1.2.5. Treatment

Of all the existing medical, nutritional and physical techniques, none actually cure OA. Treatment depends on stage/severity and mainly attempts to minimize the adverse effects on the quality of life and loss in economic productivity. The most basic method of symptom modification is non-steroidal anti-inflammatory drugs (NSAIDS). In recent years there has also been investigation of nutritional supplements with chondroitin, glucosamine, and/or hyaluronin to treat symptoms and assist in healing.

One commonly used surgical technique to simulate articular surface formation is penetration of subchondral bone. Penetration of subchondral bone in areas of advanced degeneration or complete loss of articular cartilage leads to a disruption of blood vessels in that area. This disruption causes a fibrin clot to form over the bone surface where mesenchymal stem migrate then proliferate and differentiate into cells

morphologically similar to chondrocytes. This leads to formation of a fibrocartilagenous surface with varied degrees of success [21].

Another surgical technique is to decrease articular surface contact stresses and improve joint movement to simulate articular surface restoration. This is achieved by resection of degenerated articular surfaces including some underlying bone to decrease loading and facilitate formation of fibrocartilagenous tissue.

Osteotomies are performed to decrease joint loads on severely damaged regions of articular surface in order to relieve pain and improve joint function. This is achieved by realigning and bringing into contact surfaces having some remaining cartilage. Osteotomies also help correct joint malalignment that may contribute to symptoms and joint dysfunction. This procedure is commonly used in treatment of hip and knee OA [20].

The most promising technique to date is soft tissue graft which is the introduction of a new cell population using an organic matrix. This involves bridging resected articular surfaces with perichondrial or periosteal (or other fascia) grafts. These grafts are meant to hold the cells in place in order to stimulate and facilitate generation of a new articular surface. Studies conducted thus far have shown encouraging results [20].

Proximal row carpectomy is a motion-sparing surgical procedure used to treat arthritis in the wrist [22]. This procedure is recommended for radioscaphoid arthritis, scaphoid non-union, avascular necrosis of the lunate (Kienbock’s disease) and necrosis of the scaphoid (Preiser’s disease). It involves removal of the proximal row

carpal bones scaphoid, lunate and triquetrum to create a new radiocarpal articulation between the radius and capitate. While some wrist motion is maintained, the main setback of this procedure is the loss of strength in the hand and wrist.

1.3. Modeling

Modeling is a technique that incorporates physical (scaled models) or mathematical (computational models) systems to study and investigate a research question. The advent of computers and evolution of processing power has vastly improved the study of human motion in part due to the relative ease of model construction and reduction in processing time to generate a solution. The limitations and constraints of experimental methods have elevated the use of computational methods in biomechanical studies. Computational methods are not restricted by subject variability (however, it may not be possible to generalize subject-specific models), physical limitations and risks, repeatability, environmental conditions and the like.

The entire procedure can be summarized into a few basic steps intrinsic to all modeling techniques that include creation of mechanical models, deriving the equations of motion for the models, programming a numerical solution, determining the boundary conditions and finally, interpretation and comparison with experimental data, which can be aided by precise modeling [23].

Finite element and rigid body spring modeling are the main modeling techniques currently used in biomechanical studies, the finite element method being the first of the two used in the study of the human body and the most prominent. The rigid body spring model has become somewhat popular due to its simplicity and efficiency in contact

analysis. More recently, a third technique has been developed that uses a surface-based contact approach. While maintaining computational efficiency, this provides for a more accurate interface and more flexible contact rules.

Despite the sophistication and appeal of modeling over experimental methods, there exist some key limitations that arise from factors such as numerical imperfections in the solution process, difficulty of acquiring accurate physiological material properties, approximation of complex human anatomy and *in vivo* boundary conditions.

1.3.1. Model Development

One of the key features of computational modeling is the non-invasive simulation of various loading conditions, which allows for anatomical and physiological insight, from a clinical perspective, into mechanisms of trauma and pathologies arising from acute injuries, repetitive and excessive stresses or degenerative joint diseases. Also, accurate models can provide surgeons and bioengineers with investigative tools that have the capability to increase basic knowledge while providing a new and improved approach to existing treatment procedures for better detection, prevention and cure. Therefore, accurate representation of the anatomy and material properties is vital in understanding the underlying processes leading to joint disorders.

Development of computational models for joint analysis is a complex process that begins with acquiring images of the anatomy in concern. Based on requirements, the images can contain information pertaining to bone, soft tissue or a combination of both, which are then used to generate two or three dimensional geometric models. Commonly, highly accurate X-Ray images are used for 2D models while more

advanced techniques such as Computed Tomography (CT) and Magnetic Resonance Imaging (MRI) are used to generate 3D models. CT scans are used to generate highly accurate models of bone while MRI, which has lower contrast and signal-to-noise ratio (SNR), is used to model both bone and soft tissue such as cartilage. Quality of images depends largely on the application for which they are intended.

The process of generating mechanical models involves key basic steps which are segmentation, compilation and surface mapping. Segmentation involves capturing the geometry of the anatomy of interest from individual images in the image set. Once segmentation is complete the individual contours are compiled to form a 3D point cloud. Finally, surface mapping is used to develop a surface description based on the 3D point cloud to obtain the geometric model, which along with kinematic parameters and boundary constraints is used in biomechanical analysis.

1.3.2. Rigid Body Spring Modeling (RBSM)

Bodies that are presumed non-deformable are known as rigid bodies and the rigid body theory is a fundamental and well-established theory of physics. This type of modeling is based on the assumption that bodies undergo negligible, if any, deformation when subjected to an external force. Hence, when compared to cartilage deformation at the articular surface RBSM neglects the deformation of bones (rigid bodies) constituting the joint under investigation. In biomechanical contact analysis studies, the articular surface is modeled as a series of springs in compression on the surface of bones while ligaments are modeled as springs in tension that maintain

contact. Overall, this technique is efficient to compute joint forces and tension in ligaments without the need for complex finite element analysis.

Garcia-Elias et al. conducted a study to analyze stabilizing structures of the transverse carpal arch based on RBSM theory [24]. Two dimensional models generated from MRI scans were used to determine relative motion between carpal bones, intercarpal joint compressive forces distribution and ligament tension under simulated dorsopalmar compression. Compressive springs were used to model cartilage while tensile elastic springs were used to model ligaments of the carpal arch. Results indicated the palmer hamate-capitate ligament to play a significant role in carpal arch stability.

Horii et al. used RBSM to observe the effect of various surgical procedures used to treat Kienbock's disease, on the force distribution across the carpus [25]. A 2D model of the carpus was created from CT scans and a system of compression springs used to model joint reaction forces. Spring stiffness parameters were obtained from cartilage and ligament material properties based on literature. Forces up to 143 N were applied and intercarpal displacements and loads calculated for different simulated surgical procedures. Results indicated radial shortening or ulnar lengthening to significantly unload the lunate thereby making them appropriate treatment procedures.

Schuind et al. conducted a study similar to Horii et al to investigate force transmission through the wrist using RBSM [10]. Model geometry was acquired from posteroanterior X-rays of adults with cartilage and subchondral bone represented by a

system of linear compressive springs and ligaments represented by tensile linear springs. Spring stiffness parameters were obtained from cartilage and ligament material properties based on literature and loads applied to simulate grasp strength of 10 N with active stabilization of the wrist in neutral position. Results indicated the radioscaphoid joint to transmit majority of the force (55%) with the radiolunate joint transmitting 35%. The remaining 10% was transmitted through the triangular fibrocartilage. It was found that the scaphoid bore a large percentage of the wrist load with highest peak pressure observed at its proximal pole. It was also observed that wrist morphology and age had little or no effect on magnitude and pattern of force distribution.

Iwasaki et al. used a 2D computer simulation RBSM to quantify force and pressure distributions across the wrist during different stages of Kienbock's disease [18]. Posteroanterior and lateral radiographs from 24 patients with Kienbock's were used to generate models with linear compressive springs representing articular cartilage and tensile springs representing ligaments and flexor retinaculum. Stiffness and thickness of cartilage was assumed to be constant throughout the entire articular surface. Metacarpals were loaded under a total force of 142 N and joint forces, peak pressures, ligament tensions calculated. Results indicated scaphoid rotation to play a significant role in influencing wrist joint contact pressure distribution and therefore might aid in the progression of Kienbock's disease.

Manal et al. used a novel sliding RBSM approach to study joint reaction forces in wrists affected by juvenile idiopathic arthritis (JIA) [26]. JIA leads to misalignment

of carpal bones resulting in off-center loading of the bones. Large displacements result in failure of standard RBSM due to springs representing cartilage experiencing tension instead of normal compression. This novel approach allows for sliding of springs at their distal ends along the surface of opposing bones until equilibrium is attained. Models were constructed from posteroanterior radiographs of wrists of 4 subjects with cartilage represented as linear elastic compressive springs and metacarpals loaded axially to simulate grasp required to hold a 1 kg load. Applied loads followed similar protocols as described by Schuind et al with the radius and ulna fixed, and carpal and metacarpal bones free to displace. Results indicated ratio of transmitted forces through the radiocarpal joints for healthy wrist to be similar to those reported by Horii and Schuind and wrists affected by JIA to be reasonable. The study demonstrated sliding RBSM to be an appropriate technique for estimating joint mechanics of the wrist.

Force transmission through the wrist was analyzed in the maximum extended position to clarify pathomechanics of wrist injury [27]. Three dimensional RBSM was constructed from CT scans of the wrist in neutral position and maximum extension. Ligaments were modeled as line segments with parameters acquired from literature and a total load of 140 N applied to the metacarpals in neutral and extended positions. Ligament tensions and joint forces were assumed proportional to the corresponding tensile/ compressive spring deformations. Results showed force transmission ratio to increase from neutral to extension on the scaphoid fossa and decrease on the lunate

fossa. Results showed how shifting of force transmission might play a role in wrist injuries such as scaphoid fracture.

1.3.3. Finite Element Modeling (FEM)

Current technological advancements demand the need for accurate analyses of very large and complex structural systems. Geometric irregularities, varying material properties and multiple loading conditions make accurate and efficient solutions difficult to achieve. With the magnitude of computational power available today, the process of solving a complex system can often be achieved using the finite element method.

Any complex system can be reduced to a set of small, but finite elements, which can be analyzed in combination to obtain a solution for the system as a whole. The process of reduction is known as discretization. The finite element method involves analysis of a structural system which is an assembly of a finite number of discrete elements interconnected at nodes. Once a system is described by a mesh of finite elements, it becomes easier to approximate the response of the entire system based on the behavior of the individual elements.

The FEM process can be broken down into five major steps. The process is initiated with idealization of the structural system. This involves selection of type and size of finite elements to generate a mesh of the system. Depending on computational time and accuracy of solution required one can select 1, 2, or 3D elements defined by n^{th} order polynomials. Next step is to define the geometric and elastic properties of the individual elements. This is followed by description of boundary conditions,

including definition of the loading conditions. Finally operations are performed to generate matrix equations by use of the principle of minimum energy. These matrix equations are solved to obtain displacements, strains and stresses throughout the model.

FEM generates highly accurate results and is able to provide not just surface solutions but also throughout the entire volume of analysis. It is able to simulate not only static but also dynamic loading conditions. However, depending on the complexity of system intense computation maybe involved, based on the number of elements and the order of differential equations that must be solved. This is further complicated when analyses are shifted from linear elastic to non-linear which is often the case when dealing with biological systems. Lastly, regardless of number of elements, FEM provides an approximate solution only. The higher the number of elements and polynomial order, the higher the accuracy. Hence it comes down to personal choice to balance between computational time and accuracy of solution.

Anderson et al. used a plane-strain finite element contact model to gain insight into distal radius intra-articular fracture management [28]. Contact coupled 2D FE model of the radiocarpal joint was generated from scaled anatomic drawings of the distal radius, lunate and scaphoid bones. 1291 quadrilateral elements were used to create the FE mesh with material properties based on known values from literature. Ligamentous attachments were modeled using nonlinear spring elements with stiffness properties based on Horii et al. No assumptions were made regarding load transfer across contact surfaces as these can be determined iteratively using the

contact coupled FE method. Contact was modeled using slideline elements, which allow finite sliding and deformations between bodies, and coulomb friction as the contact criteria. Coefficient of friction of 0.01 was chosen for all articular surfaces. Results indicated load distribution between radius and ulna to compare well with previous data. The plot of axial strain verified the role of articular cartilage in load distribution and strains were on the order of 20 to 25%. Stress distributions were also consistent with previous studies and it was concluded that the model shows promise in fulfilling the intended hypothesis.

Ulrich et al. conducted a study that used computational models and high resolution images to quantify load transfer through distal radius trabecular network *in vivo* and to explain the effects of tissue loads leading to fracture in those regions [29]. High resolution images (165 μm) of the left distal radius and adjacent carpal bones were taken using a low-dose peripheral quantitative 3D CT scanner from which FE models were created using the voxel conversion technique. The entire FE mesh consisted of 1,679,025 elements and all material properties including cartilage thickness of 3 mm, were acquired from literature. Different load ratios were used to load the carpal bones to signify two hand positions during impact, namely neutral and ulnar/radial deviation. Tissue strain energy density distribution was used to illustrate load transfer through the trabecular network. This method showed that characterization of tissue load distribution *in vivo* is feasible. Results indicated radius to have high strain energy values for all loading cases and this suggests that common

regions of fracture are dependant on high tissue strain energy density values in the trabecular network.

Ledoux et al. investigated mechanisms of modifications to the mechanical behavior of the carpus after a scaphoid fracture that might result in the onset of arthritis of the wrist [30]. Two dimensional FE model of the wrist was generated from an anteroposterior X-ray image of the wrist in pronated position. The trapezium and the trapezoid were modeled as a single bone while the pisiform was not modeled at all. FE mesh generated was defined by 1053 nodes with non-linear properties assigned to ligament and cartilage elements. All fracture simulations were loaded at 100 N at the level of both radius and ulna. The study showed existence of pressure peaks at the nonunion and midcarpal (scaphoid-capitate and lunate-capitate) interface which explains the progression of nonunion of the scaphoid leading to arthritis of the wrist. The study also showed a shift in pressure distribution on articular surfaces after the occurrence of a fracture.

Carrigan et al. performed a study to analyze load transmission in the carpus during static compressive loading using a 3D FEM in static neutral position [31]. Geometry was obtained from in vivo CT scans of the carpal and metacarpal bones along with the radius and ulna. Meshes were generated for individual bones and compiled in ANSYS to assemble carpal geometry. Triangular prism elements were used for cartilage layers while non-linear spring elements were used to model ligaments and material properties (linear elastic) were defined based on prior FE studies. A 15 N compressive load was applied to the capitate for all cases and a series

of parametric sensitivity cases analyzed to determine impact of various factors on contact pressures and cartilage stresses. Cartilage material modulus and unconstrained carpal rotation were found to have the greatest impact on contact area and pressure distribution (contact pressure and principle compressive stress).

A simplified adaptive meshing technique was developed to facilitate FE analysis of a dual-curvature total wrist implant [32]. While current FE programs provide adequate flexibility in mesh generation, element sizes and spacing have to be defined in advance. This is an iterative procedure that may or may not generate acceptable solutions. Adaptive meshing improves accuracy by allowing for dynamic and continuous refinement (increase/ decrease in size or order of elements) depending on analysis. While several custom adaptive meshing FE codes have been created, this study developed a formulation compatible with pre-existing commercial programs. Preliminary solution was initially determined on base mesh for a series of time steps. Using an error indicator, regions requiring greater mesh resolution were located and based on a centralized element, finer grids adaptively created. The technique was validated by testing two dislocations (volar and rotational) of the total wrist implant. Refinements showed a substantial decrease in error thereby demonstrating the effectiveness of this method.

Nonlinear FEM was used to analyze biomechanical interactions of various fixation techniques for distal radius fracture under different loading conditions [33]. CT scans were used to generate a 3D distal radius fracture FE model. Meshes were generated comprising 72,545 to 95,988 elements for the different fixation simulations

and cortical and cancellous bones modeled as linear elastic and isotropic. Material properties were based on, and model validated by comparison with experimental data obtained from prior FE studies. Double-plating, modified double-plating and single plating fixation methods were analyzed under axial, bending and torsion loads. Results showed modified double-plating as the better choice in distal radius fracture fixation because of high rigidity and least displacement in bending. Also, lower stresses indicated better structural strength against bending with minimum possibility of fragmentation and screw loosening.

A study was conducted to understand the impact of bone mineral density (BMD) and direction of loading on distal radius fracture strength and initiation location [34]. Three dimensional FE model of the radius, scaphoid and lunate was constructed from CT scans of the right wrist of a 53 year old female positioned at 57° flexion and 7° ulnar deviation to simulate extreme impact. The model comprised of hexahedral and tetrahedral elements and material properties, acquired from literature, assumed as linear isotropic while ligaments were modeled as nonlinear springs. The model was validated by comparing contact area and peak contact stress with experimental data from previous studies. Results showed changes in BMD to cause similar changes in fracture strength while modifying loading direction caused a marginal decrease in fracture strength. It was suggested that increasing the extent to which radius is axially loaded could benefit Colles' fracture intervention methods.

A finite element model was used to study the effect of wire positioning on initial stability of scaphoid fractures [35]. An FE model of the scaphoid and corresponding

joints was generated. Five different two-wire configurations using Kirschner wires were used to simulate scaphoid waist fracture fixation. Models were analyzed for three different coefficient of friction values and a 200 N load applied. Results showed that fixation stability is increased by crossing of wires not only in the frontal plane, but also in the plane perpendicular to the hand.

1.3.4. Multi Body Contact Modeling

Contact modeling is a powerful procedure used for complex structural analysis of rigid or deformable interacting bodies, based on a contact rule. Various programs exist that can model a broad range of systems. The most attractive feature of contact modeling is the ability to generate solutions more quickly than FE methods, using highly efficient algorithms. Also, contact modeling does not make a priori assumptions about details of load transfer across joint surface. The nature and distribution of these loads are determined from the computations involved in the contact model [28]. Hence, this technique has been shifted to encompass biomechanical systems as well, including diarthrodial joint modeling. The main drawback is the restriction of analyses to contact parameters, as opposed to stresses and strains throughout the solid that may be obtained using FEM.

Kwak et al. developed an algorithm for 3D quasi-static analysis of multi body systems, especially tailored for diarthrodial joints [36]. The program is able to accommodate articular contact, muscle, tendon and ligament forces and soft tissue wrapping around bone and cartilage surfaces. Material bodies, bones for example, were modeled having six degrees of freedom (three rotation, three translation) while

particles imbedded in soft tissue, representing tendons and ligaments, were assigned three translational degrees of freedom. The imbedded particles are responsible for redirecting ligament or tendon forces while transmitting resultant contact force to the body around which they are wrapped. Ligaments were modeled as links connecting insertion points on distinct bodies along a series of line segments, with forces acting along the direction of the line. Muscles were modeled as special cases of ligament links and forces were simulated by a constant force applied on a line segment inserted into separate bodies. Surface contact link was used to simulate articular surface contact with contact region defined by a proximity function, that is, an overlap of rigid surfaces. The models were implemented using input files containing geometric entities and link parameters, with several options including force-displacement ligament models and linear/ non-linear cartilage deformation models. Cartilage and bone surfaces were represented as triangular facets along with the use of analytical Jacobians for computational efficiency. Contact pressures were determined by surface interpenetration of points between adjacent bodies. Results were within prescribed convergence criteria and were further validated using patellofemoral joint models constructed from six cadaver knees.

Pillai et al. conducted a study to evaluate *in vivo* wrist joint contact mechanics using MRI based contact modeling [37]. Model geometry was acquired from MRI scans of the non-dominant wrist of four human subjects using a 1.5 Tesla clinical MRI scanner with a flex coil. Scans were performed during light active grasp of a 30 mm cylinder and during relaxed state with the forearm in neutral position. Wrist

position during grasp was not strictly controlled. Manual segmentation of the radius and carpal bones (lunate and scaphoid) including articular surfaces was performed on the relaxed image sets to obtain contour data which were then used to generate 3D surface models. The three bones, excluding articular surfaces, were isolated from the grasp and relaxed image sets in order to determine transformations from the unloaded to loaded configuration. Using the radius as a fixed reference, surface registration was performed to obtain kinematics (rotation and translation vectors) for both lunate and scaphoid. The kinematic parameters along with geometric entities were implemented into a multi body contact program based on Kwak et al for contact analysis. Contact rule was defined for cartilage thickness of 1 mm and material properties acquired from literature. *In vivo* contact pressures, areas and forces were analyzed for each articulation and found to be reasonable when compared with previous studies. This study showed MRI based contact modeling to be a useful tool in evaluating *in vivo* joint contact mechanics.

Thoomukuntla performed a study to validate the MRI based modeling approach developed by Pillai et al. [38]. Model geometry was acquired from MR scans of the wrist of three cadaver forearm specimens. Volar dissection of the wrist was performed to insert pressure (static film and electronic) sensors for direct measurements while three flexor tendons (FDS, FDP and FPL) were isolated to simulate light grasp when loaded. The forearms were attached to a base plate to maintain neutral rotation. Direct measurements were taken by inserting pressure sensors into dissected joint space and loading the tendons in light grasp. Similarly,

MR scans of the wrist were taken in relaxed and loaded configuration, which were used to generate 3D models. Using the radius as a fixed reference, kinematic transformations of the carpal bones from the unloaded to the loaded states were obtained. These along with the models, were loaded into a contact modeling software (Kwak et al) for contact analysis. Results compared between pressure sensors and MRI based models were reasonable. Also, contact areas were directly measured from MR scans and these were found to match closely with model results.

Waller further validated the technique proposed by Pillai et al. and Thoomukuntla et al. [39]. Five cadaver forearm specimens were used and similar procedure followed based on Thoomukuntla. In this instance five tendons (two extensors and three flexors) were isolated for joint loading. After kinematic and contact analyses, results obtained from models were significantly similar to direct contact area measurements from MR scans, contact forces similar to Tekscan measurements and peak pressures similar to Pressurex measurements. These results further validated the MRI based modeling technique to be feasible for joint contact analysis and this approach will therefore form the basis of this study.

1.4. Validation Methods

Several experimental methods have been proposed and used in literature for measuring radiocarpal contact mechanics. While each method is subject to restrictions and limitations, they prove useful in providing data for comparison with computational modeling methods and thereby assist in their validation.

1.4.1. Published Pressure Sensor Data

Tencer et al. conducted a study to determine pressure distribution across the radiocarpal joint [9]. Five cadaver forearm specimens were used and incisions made to the dorsal wrist joint space in order to insert a Fuji pressure sensitive film that was made to conform to the articulating surface. A special setup was used for joint axial loading and 36 positions tested, which combined flexion/ extension with radioulnar deviation and pronation/ supination. A compressive load of 103 N was applied using dead weights across the second and third metacarpals. For this load, peak pressure averaged 3.17 MPa and scaphoid contact area found to be 1.47 times that of lunate, which varied with position.

Kazuki et al. studied variations in radiocarpal joint pressure distribution between normal wrists and simulated malunited Colles' fractures [14]. Four cadaver forearm specimens were used and dorsal radiocarpal joint capsule partially dissected to insert a Fuji super low-pressure film. A total load of 100 N was applied to the wrist across the third metacarpal and tested for 27 forearm positions. Results showed average peak radioscaphoid and radiolunate pressures to be 2.8 and 2.7 MPa respectively. For simulated Colles fracture results showed decreased contact areas and volar to dorsal shifts in location with increased deformation.

Wilson et al. conducted a study to determine the accuracy and repeatability of an I-scan system (Tekscan Model #5051) for measuring forces and pressures [40]. The system operates by relating changes in electrical resistance to an applied force. The system was calibrated and accuracy assessed by applying known forces and force

distributions across the sensor using a setup in a materials testing machine. For five trials at seven load levels, the sensor was accurate to within 6.5%. Repeatability was assessed based on measurements obtained from patellofemoral contact analysis using four cadaver specimens loaded in continuous and static flexion. Results for forces and force distributions showed 2.2 to 9.1% variability in measurement. Thus, it was concluded that the Tekscan system was comparable to the Fuji film in terms of accuracy and repeatability and was superior in terms of geometry, accuracy of contact area measurement and dynamic force, pressure and area measurement.

Wilson et al. performed a similar study to the one mentioned above in the lumbar spine facets of four cadaver specimens [41]. Repeatability was assessed by loading in axial rotation and flexion-extension (five trials) and accuracy assessed by applying known compressive loads and comparison with measured loads. Results showed repeatability for all measurements to be within 4-6% for axial rotation and 7-10% for extension while accuracy was highly dependent on calibration protocol and sensor measurement range.

Harris et al. [42] and Bachus et al. [43] both conducted studies to compare measurements recorded from pressure sensitive films and piezoelectric pressure sensors. Harris et al looked at contact areas in total knee arthroplasty (TKA) devices using a custom TKA setup that allowed freedom of motion in any loading configuration. Tekscan and Fuji film were used to measure contact areas at 0-110° flexion with loads multiple times body weight. Fuji films were found to measure 11-36% lower contact areas than Tekscan. Similarly, Bachus et al compared area, force

and pressure measurements. These were measured between a cylindrical peg and a base plate compressed with known loads. Results indicated all measurements for both sensors to fall outside the hypothesized accuracy value (+/-5% of known load values) although Tekscan was found to be more accurate when estimating area and pressure.

1.4.2. Model Validation

Song et al. calculated anterior cruciate ligament (ACL) forces using an experimentally validated 3D FE model [44]. Experimental kinematics and in situ forces were determined in a cadaver knee for a full extension to 90° flexion using a robotic/ UFS testing system. Tibial loads ranging from 0 to 134 N were applied to the knee at full extension and resulting kinematics recorded. 3D FE model of the ACL, femur and tibia was generated from MR scans of the knee with ACL bundle insertion sites obtained using Microscribe. Ligaments were assigned homogeneous and isotropic hyperelastic material properties as anisotropic material properties were unavailable. Boundary conditions were based on experimentally obtained kinematics. Results indicated difference between in situ experimental and calculated force data to be less than 11%. The validated FEM was then used to determine force and stress distribution within the ACL.

Anderson et al. validated patient-specific contact FE models using a high resolution pressure sensor [45]. Model geometry was acquired from CT scans of two cadaver ankle specimens loaded in neutral flexion/ extension. The ankle joints were loaded in a materials testing machine with a compressive load of 600 N. An FE mesh of 2997 to 293402 elements was created to generate models. Linear isotropic material

properties were assigned along with boundary conditions to replicate experimental loading. Contact stress distributions were compared between experimental and computational results. Validation was based on direct comparison with physical measurements from corresponding cadaver loading tests. The contact stress and contact area comparisons were reasonable while pixel-by-pixel comparisons of stress distribution across articular surface showed considerable agreement. Direct comparisons between physical measurements and model during ankle loading were said to have validated the model.

Papaioannou et al. used biplane dynamic Roentgen stereogrammetric analysis (DRSA) coupled with Tekscan sensor to validate specimen-specific knee joint FE models [46]. Models were constructed from CT scans of three cadaver knees with eight-node trilinear hexahedral elements having linearly elastic and transversely isotropic material properties. The experimental setup consisted of the knees mounted in a custom system designed to operate as a special application materials testing machine. This system allowed axial tension/ compression and synchronous planar translation in the transverse plane. Experimental results were obtained from a Tekscan sensor attached to tibia plateaus using an arthroscopic procedure along with high-speed kinematics measured with DRSA. Convergence of FE solution indicated accuracy while confidence in model validity itself was achieved by comparison of contact variables with direct experimental measures. Models were found to predict most of the contact variables measured experimentally (average RMS error of 0.91).

Anderson et al. conducted a study to validate a finite element model to predict cartilage contact pressure in the human hip joint [47]. Subject-specific geometry acquired from CT image data was used to construct the FE model. *In vivo* loading data was used to simulate walking, descending stairs and stair climbing. Experimental data was acquired using low range pressure sensitive film. Misalignment errors between FE and experimental results and differences in magnitude of contact between model and experimental results were investigated. Results showed misalignment errors (difference in RMS error before and after alignment of FE results) to be less than 10% while magnitude errors (residual errors following alignment) were approximately 30%. The model was considered validated as the FE predictions compared favorably with experimental measurements and published experimental data.

Clearly, the best validation approach is specimen-specific data comparison, as opposed to a comparison to similar data found in the literature. Curiously, many models are proposed and used in studies without *any* real validation criterion [45]. For our proposed imaging-modeling approach we chose specimen-specific validation!

Because of the variability in experimental measures, the validation criterion was data falling within 2 times the *average* accuracy of the measurement system.

1.5. References

1. Harty, M., The hand of man. Phys Ther 1971;51(7):777-81.
2. Hazelton, F., Smidt, G., Flatt, A., Stephens, R., The influence of wrist position on the force produced by the finger flexors. J Biomech 1975;8(5):301-6.
3. Simpson, D., The functioning hand, the human advantage. J R Coll Surg Edinb 1976;21(6):329-40.
4. Drobner, W.S., Hausman, M.R., The distal radioulnar joint. Hand Clin 1992;8(4):631-44.
5. Kapandji, A., Biomechanics of pronation and supination of the forearm. Hand Clin 2001;17(1):111-22.
6. Palmer, A.K., Werner, F.W., Biomechanics of the distal radioulnar joint. Clin Orthop Relat Res 1984;(187):26-35.
7. Rabinowitz, R.S., Light, T.R., Havey, R.M., Gourineni, P., Patwardhan, A.G., Sartori, M.J., Vrbos, L., The role of the interosseous membrane and triangular fibrocartilage complex in forearm stability. J Hand Surg [Am] 1994;19(3):385-93.
8. Pfaeffle, H.J., Fischer, K.J., Manson, T.T., Tomaino, M.M., Herndon, J.H., Woo, S.L., A new methodology to measure load transfer through the forearm using multiple universal force sensors. J Biomech 1999;32(12):1331-5.
9. Tencer, A.F., Viegas S.F., Cantrell, J., Chang, M., Clegg, P., Hicks, C., O'Meara, C., Williamson, J.B., Pressure distribution in the wrist joint. J Orthop Res 1988;6(4):509-17.

10. Schuind. F., Cooney, W.P., Linscheid, R.L., An, K.N., Chao, E.Y., Force and pressure transmission through the normal wrist. A theoretical two-dimensional study in the posteroanterior plane. J Biomech 1995;28(5):587-601.
11. Lieber, R.L., Friden, J., Musculoskeletal balance of the human wrist elucidated using intraoperative laser diffraction. J Electromyogr Kinesiol 1998;8(2):93-100.
12. Kobayashi, M., Berger, R.A., Linscheid, R.L., An, K.N., Intercarpal kinematics during wrist motion. Hand Clin 1997;13(1):143-9.
13. Nowalk, M.D., Logan, S.E., Distinguishing biomechanical properties of intrinsic and extrinsic human wrist ligaments. J Biomech Engr 1991;113(1):85-93.
14. Kazuki, K., Kusunoki, M., Shimazu, A., Pressure distribution in the radiocarpal joint measured with a densitometer designed for pressure-sensitive film. J Hand Surg [Am] 1991;16(3):401-8.
15. Rettig, A.C., Management of acute scaphoid fractures. Hand Clin 2000;16(3):381-95.
16. Romdhane, L., Chidgey, L., Miller, G., Dell, P., Experimental investigation of the scaphoid strain during wrist motion. J Biomech 1990;23(12):1277-84.
17. Ruby, L.K., Wrist biomechanics. Instr Course Lect 1992;41:25-32.
18. Iwasaki, N., Genda, E., Minami, A., Kaneda, K., Chao, E.Y., Force transmission through the wrist joint in Kienbock's disease: a two-dimensional theoretical study. J Hand Surg [Am] 1998;23(3):415-24.
19. Praemer, A., Musculoskeletal conditions in the United States. American Academy of Orthopedic Surgeons, Rosemont, IL, 1999.

20. Buckwalter, J.A., Martin, J.A., Osteoarthritis. Adv Drug Deliv Rev 2006;58(2):150-67.
21. Buckwalter, J.A., Martin, J.A., Olmstead, M., Athanasiou, K.A., Rosenwasser, M.P., Mow, V.C., Osteochondral repair of primate knee femoral and patellar articular surfaces: implications for preventing post-traumatic osteoarthritis. J Orthop 2003;23:66-74.
22. DiDonna, M.L., Kiefhaber, T.R., Stern, P.J., Proximal row carpectomy: study with a minimum of ten years of follow-up. J Bone Joint Surg [Am] 2004;86-A(11):2359-65.
23. Andriacchi, T.P., Mikosz, R.P., Hampton, S.J., Galante, J.O, Model studies of the stiffness characteristics of the human knee joint. J Biomech 1983;16(1):23-9.
24. Garcia-Elias, M., An, K.N., Cooney, W.P., Linscheid, R.L., Chao, E.Y., Transverse stability of the carpus. An analytical study. J Orthop Res 1989;7(5):738-43.
25. Horii, E., Garcia-Elias, M., Bishop, A.T., Cooney, W.P., Linscheid, R.L., Chao, E.Y., Effect on force transmission across the carpus in procedures used to treat Kienbock's disease. J Hand Surg [Am] 1990;15(3):393-400.
26. Manal, K., Lu, X., Nieuwenhuis, M.K., Helders, P.J., Buchanan, T.S., Force transmission through the juvenile idiopathic arthritic wrist: a novel approach using a sliding rigid body spring model. J Biomech 2002;35(1):125-33.
27. Majima, M., Horii, E., Matsuki, H., Hirata, H., Genda, E., Load transmission through the wrist in the extended position. J Hand Surg [Am] 2008;33(2):182-8.

28. Anderson, D.D., Daniel, T.E., A contact-coupled finite element analysis of the radiocarpal joint. Semin Arthroplasty 1995;6(1):30-6.
29. Ulrich, D., van Rietbergen, B., Laib, A., Ruegsegger, P., Load transfer analysis of the distal radius from in-vivo high-resolution CT-imaging. J Biomech 1999;32(8):821-8.
30. Ledoux, P., Lamblin, D., Targowski, R., Modifications to the mechanical behavior of the wrist after fracture of the scaphoid. Modeling by finite element analysis. Acta Orthop Belg 2001;67(3):236-41.
31. Carrigan, S.D., Whiteside, R.A., Pichora, D.R., Small, C.F., Development of a three-dimensional finite element model for carpal load transmission in a static neutral posture. Ann Biomed Eng 2003;31(6):718-25.
32. Roarty, C.M., Grosland, N.M., Adaptive meshing technique applied to an orthopaedic finite element contact problem. Iowa Orthop J 2004;24:21-9.
33. Cheng, H.K., Lin, C., Lin, Y., Chen, A.C., Biomechanical evaluation of the modified double-plating fixation for the distal radius fracture. Clin Biomech 2007;22(5):510-7.
34. Troy, K.L., Grabiner, M.D., Off-axis loads cause failure of the distal radius at lower magnitudes than axial loads: a finite element analysis. J Biomech 2007;40(8):1670-5.
35. Ezquerro, F., Jimenez, S., Perez, A., Prado, M., de Diego, G., Simon, A., The influence of wire positioning upon the initial stability of scaphoid fractures fixed using Kirschner wires: a finite element study. Med Eng Phys 2007;29(6):652-60.

36. Kwak, S.D., Blankevoort, L., Ateshian, G.A., A Mathematical Formulation for 3D Quasi-Static Multibody Models of Diarthrodial Joints. Comput Methods Biomech Biomed Engin 2000;3(1):41-64.
37. Pillai, R.R., Thoomukuntla, B., Ateshian, G.A., Fischer, K.J., MRI-based modeling for evaluation of in vivo contact mechanics in the human wrist during active light grasp. J Biomech 2007;40(12):2781-7.
38. Thoomukuntla, B.R., McIff, T.E., Ateshian, G.A., Bilgen, M., Toby, E.B., *Fischer, K.J*., Preliminary validation of MRI-based modeling for evaluation of joint mechanics. Journal of Musculoskeletal Research (*in press*).
39. Waller, A.J., Master's Thesis: Refinement and validation of MRI-based models for joint contact mechanics. Mechanical Engineering, University of Kansas, 2007.
40. Wilson, D.R., Apreleva, M.V., Eichler, M.J., Harrold, F.R., Accuracy and repeatability of a pressure measurement system in the patellofemoral joint. J Biomech 2003;36(12):1909-15.
41. Wilson, D.C., Niosi, C.A., Zhu, Q.A., Oxland, T.R., Wilson, D.R., Accuracy and repeatability of a new method for measuring facet loads in the lumbar spine. J Biomech 2006;39(2):348-53.
42. Harris, M.L., Morberg, P., Bruce, W.J., Walsh, W.R., An improved method for measuring tibiofemoral contact areas in total knee arthroplasty: a comparison of K-scan sensor and Fuji film. J Biomech 1999;32(9):951-8.

43. Bachus, K.N., DeMarco, A.L., Judd, K.T., Horwitz, D.S., Brodke, D.S., Measuring contact area, force, and pressure for bioengineering applications: using Fuji Film and TekScan systems. Med Eng Phys 2006;28(5):483-8.

44. Song, Y., Debski, R.E., Musahl, V., Thomas, M., Woo, S.L., A three-dimensional finite element model of the human anterior cruciate ligament: a computational analysis with experimental validation. J Biomech 2004;37(3):383-90.

45. Anderson, D.D., Goldsworthy, J.K., Li, W., Rudert, M.J., Tochigi, Y., Brown, T.D., Physical validation of a patient-specific contact finite element model of the ankle. J Biomech 2007;40(8):1662-9.

46. Papaioannou, G., Nianios, G., Mitrogiannis, C., Fyhrie, D., Tashman, S., Yang, K.H., Patient-specific knee joint finite element model validation with high-accuracy kinematics from biplane dynamic Roentgen stereogrammetric analysis. J Biomech 2008;41(12):2633-8.

47. Anderson, A.E., Ellis. B.J., Maas, S.A., Validation of finite element predictions of cartilage contact pressure in the human hip joint. J Biomech Eng 2008;130(5):051008.

2. Effect of Film

2.1. Background

In orthopaedic Biomechanics, experimental *in vitro* studies are performed to investigate various kinds of joint and tissue mechanics and to validate computational models. Several techniques exist to determine in situ joint contact measurements, the broad categories being pressure sensitive films and electronic pressure sensors. These sensors are inserted directly into joint space under investigation, while the joint is under load, to measure contact pressure distributions, forces and areas.

Pressure sensitive films along with piezoelectric (both conductive and resistive) sensors have been used widely in literature for contact analysis of various joints such as ankle, knee, spine and wrist [1-7]. Tekscan sensors are the common electronic sensor of choice due to their dynamic real-time measurements and are available in a wide variety of models for various applications. For pressure films, Pressurex Fuji-scale film sensors are a common choice due to their high spatial resolution and are also available in a number of pressure ranges for different applications.

While pressure sensors used in biomechanical studies are designed to be as minimally intrusive as possible, geometric and material properties can result in undesired effects. Super-Low-Fuji-scale Pressurex film, has a total effective thickness of 0.3 mm and an average effective elastic modulus of approximately 100 MPa in compression [8]. This thickness is comparable to cartilage found in joints of small animals and 30% of articular cartilage thickness in some human joints. Also, the elastic modulus is an order of magnitude greater than human articular cartilage elastic

modulus. Wu et al used finite element models to study the influence of inserting Fuji film into articular joints on the contact mechanics [8]. Sensor and cartilage were modeled as linear elastic and biphasic, respectively. Depending on loading conditions, joint geometry and cartilage mechanical properties, presence of film increased peak contact pressures by 10 – 26 percent. Taking this into consideration, along with film accuracy (10% approximately), it was concluded that errors in joint contact pressure measurements could be as high as 14 – 28 percent. A similar study was conducted by Liau et al to determine effect of Fuji film on contact characteristics in an artificial tibiofemoral joint [9-10]. Two and three dimensional finite element models were used to simulate contact with and without film and contact characteristics were determined. Presence of film in joint space was found to alter original contact behavior. Contact area measurements were overestimated by 14 – 77% while contact pressure measurements were underestimated by 8 – 14%.

While the effect of a thin film sensor in the joint has been characterized, as above, the effects may vary considerably with application. Thus, experimental MRI data was acquired with and without Pressurex Super Low film in the radiocarpal joint during loading. The purpose of this study was to determine the effect of inserting a pressure sensor (specifically, the Pressurex film) into joint space on radiocarpal contact area, contact force, pressure distribution and peak pressures. The effect was measured by comparing results of MRI-based models of the normal joint (without film) and joint with film inserted.

2.2. Methodology

2.2.1. Specimen and Experimental Setup

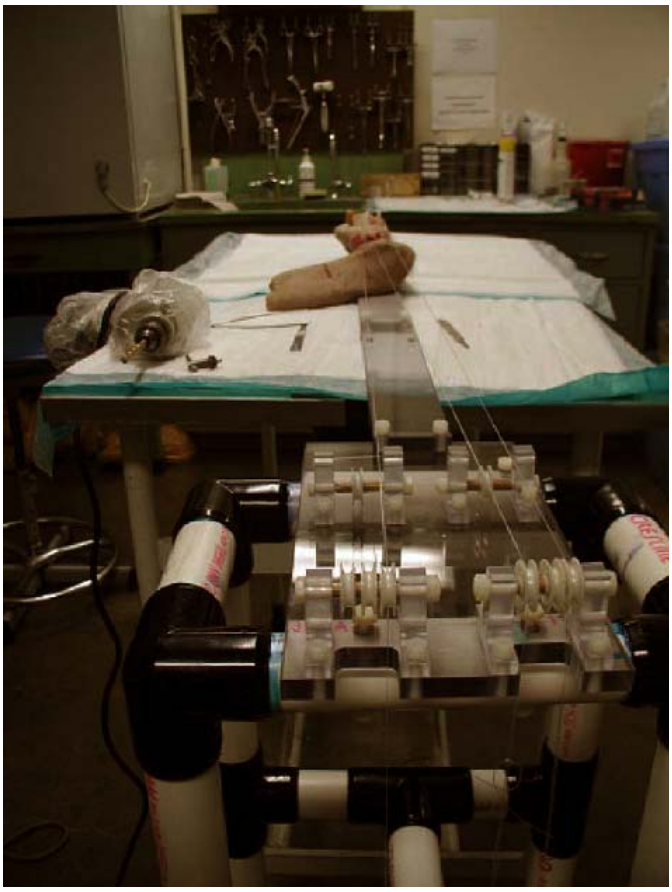

Figure 2.1 Showing mounted specimen and test rig for joint loading.

A single cadaver forearm specimen was used for this study and dissection involved isolation of bones and tendons of concern along with volar dissection of the radiocarpal joint capsule for sensor insertion. Initially, the three wrist flexors (FDS, FDP and FPL) and two extensors (ECU and ECR) were isolated [11]. Once isolation was completed, tendons were wrapped in saline soaked gauze to prevent drying and loss of function. Suture loops were attached to all isolated tendons to allow tensile loading. Soft tissue was removed along a 10 cm length of the forearm, 2 cm proximal

to the joint and extending proximally to expose the radius and ulna. Two 6.35 mm holes were drilled through the radius and one through the ulna to attach the specimen to a base plate using plastic threaded bolts. It was ensured that the holes were aligned in a manner so as to maintain forearm neutral rotation for the duration of testing and imaging.

For MRI compatibility, only non-ferrous materials were used in the experimental setup. The test rig along with side components were fabricated entirely from plastic. The pulley system was attached to the stand which provided a stable platform for joint loading. Connecting plates of variable lengths were used to interconnect the base plate and loading stand depending on the desired placement within the MRI scanner. Static load was applied using water jugs, pre-filled and weighed for a known load, and connected with the help of a pulley system to the tendons via 40 lb (178 N) fish lines (Fig. 2.1). Loading both the flexors and extensors provided a more realistic simulation of light grasp. A total of 110 N was applied to the joint to simulate light grasp [11]. This was distributed as 30 N applied to both ECU and ECR, 20 N applied to both FDP and FDS while the FPL was loaded with 10 N. Before load application, a cylindrical PVC pipe (1.5 inch outer diameter) was placed in the hand as an object for simulated grasp. Fingers were taped around the pipe to maintain position without tendon loads. To maintain wrist stability extensors were loaded first, followed by the flexors.

MRI data of the wrist was acquired under three different conditions: 1) without load on the wrist, 2) during simulated grasp (with 110 N of extrinsic tendon force

across the wrist), and 3) during simulated grasp with Pressurex Super-Low-Fuji-scale film in the radiocarpal joint.

2.2.2. MR Data Acquisition

Anatomical geometry and boundary conditions for the models were obtained from MRI scans of the wrist. These scans were performed using a 9.4 Tesla MRI scanner (Unity INOVA Animal Systems, Varian Inc., Palo Alto, CA). The wrist scans were first acquired with no load on tendons or wrist joint (unloaded/relaxed). Subsequently images were acquired during simulated light grasp as described above (loaded). Finally, images were acquired during simulated grasp with Fuji-scale-Super-Low film inserted in the joint space (loaded with film). All scans were performed for a TR of 800 ms, TE of 7.81 ms, flip angle of 45° and 4 averages. The image sizes were 1024 × 512 pixels with a 140 × 70 mm FOV. The in-plane resolution was 0.14 mm. Unloaded scans had 56, 1 mm thick slices and slice increment of 0.5 mm (0.5 mm overlap). Both loaded scans had 28, 1 mm thick slices and 1 mm offset (no overlap).

2.2.3. Model Construction

In order to measure effect of film on radiocarpal contact mechanics, two sets of models were constructed. One was the original model of the normal joint and the second model was constructed in a manner to simulate presence of film in the joint space (expanded size model).

Unloaded scans were manually segmented using MPXImage (Ted Manson, 1998, University of Pittsburgh) to obtain radius and carpal bone geometry including cartilage. Contours of the bones in all relevant scans were defined using Bezier

splines, and the corresponding points were written to a file. These 2D points were compiled into 3D point cloud and converted into surface models using Geomagic Studio 9 (Raindrop Geomagic. Research Triangle Park, NC). Original models were representative of respective bone and cartilage. These models were implemented with kinematics from the loaded scans without film. For scans with film, bone models had to be modified to account for presence of film within joint space. This was achieved by scaling the models to add half the film thickness on all bone surfaces such that contact would occur when the models were separated by the film thickness. The Super Low Pressurex film used for the study was 0.007 in (0.1778 mm) thick. Individual models were scaled uniformly about their centroids in Geomagic by specifying a scale factor. Using an iterative procedure incorporated in a MATLAB (Mathworks Inc., Natick, MA) code, distances between similar points comparing original and scaled models were checked (for entire geometry) until they were all within 0.6 – 0.8% of half film thickness. The scaled models (Fig. 2.2) were then used for contact analysis.

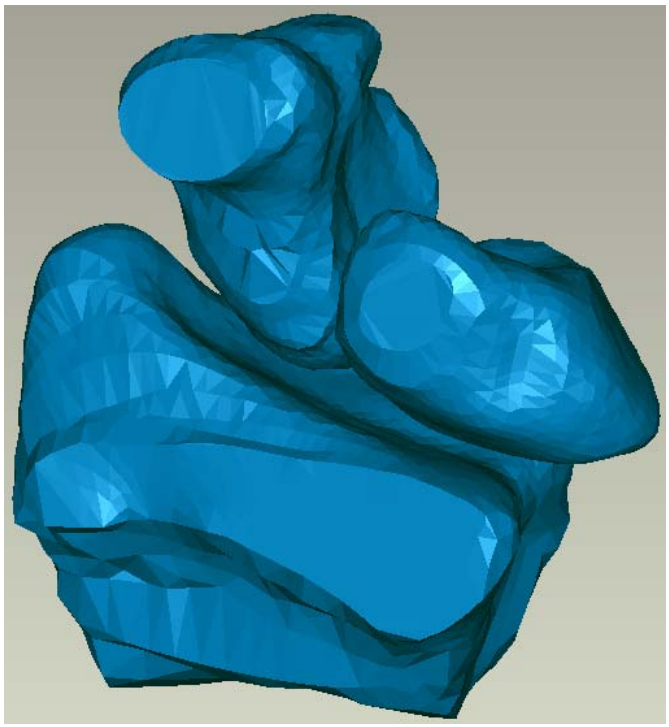

Figure 2.2 3D scaled surface model of the radiocarpal joint.

2.2.4. Registration and Kinematic Analysis

For kinematic analysis, it was assumed that bone deformation was negligible compared to cartilage deformation. Hence bone geometry alone was used for image registration to obtain the kinematic boundary conditions. Images showing respective bones were isolated in Adobe Photoshop 6.0 (Adobe Systems Inc, San Jose, CA). This was achieved by removing all surrounding detail around the bone in question and replacing with a black background. The isolated unloaded and loaded (with and without film) image sets were imported into Analyze 5.0 (AnalyzeDirect, Overland Park, KS) for registration. The image sets were compiled into individual volumes and 3D-voxel based registration was performed (similar to the procedure of Waller, 2007).

The radius was selected as the fixed reference and registration of loaded radius to unloaded radius provided the transformation between the volume loaded without film to the volume unloaded without film. This was repeated for loaded with film to unloaded without film. Thus both loaded image sets were registered to the unloaded image set. For the registration, 25 trials were performed to select best transformation based on either convergence or the average of registration behavior as judged by translation vector magnitude. The selected transformations were then used to transform the loaded carpal bone image volumes (whether with or without film) into the unloaded image coordinate system. The final step was to register unloaded carpal bones to transformed loaded carpal bones to obtain kinematics from the unloaded to the loaded configuration. Thus, for example, the unloaded scaphoid was registered to the transformed loaded scaphoid from images without film for the standard kinematics and registered to the transformed loaded scaphoid from images with film for effect of film kinematics. The same criteria (as for the radius) were used to select the best and final transformation for each bone. Final carpal bone kinematics were then implemented in the contact analysis software. Prior to implementation into the contact program, carpal kinematics were corrected from the Analyze left-hand coordinate system and expressed as attitude and translation vectors determined from transformation matrix [12].

2.2.5. Contact Analysis

The Joint_Model program (Kwak et al., Columbia University, 2000) was used for contact analysis. This is computationally efficient software that allows for modeling

of multiple rigid bodies with 3D articular contact. Local interpenetration approximated articular deformation and contact area was the area of surface penetration. Contact pressure was proportional to local surface penetration and cartilage material properties, and it was displayed as color intensity. Cartilage was assigned uniform thickness of 1 mm and elastic modulus of 4 MPa [13]. Contact forces were determined by integrating contact pressure with respect to contact area.

Body geometries, contact parameters and boundary conditions were specified in an input file for Joint_Model. The CTPSTRL contact rule was chosen which modeled contact pressure as proportional to strain (ratio of local penetration to the sum of cartilage thicknesses). The radius was kept fixed and kinematics were applied to the carpal bones. Joint_Model calculated solutions iteratively for a maximum penetration depth of 2 mm (1 mm on either articular surface). Contact analysis was used to determine peak contact stresses, contact forces, contact areas and contact pressure distributions on the articulating pair surfaces.

2.3. Results

2.3.1. Kinematic Analysis

Table 2.1 and Fig. 2.3 show kinematics obtained from registration with and without the presence of film in the radiocarpal joint. Results showed higher lunate translations and rotations (magnitudes) when compared with scaphoid. Looking at translation magnitudes, both lunate and scaphoid showed higher values with film than without film (20.7 and 15.7% respectively). On the other hand, only lunate had higher value (16.9%) for rotation magnitudes with the presence of film. Scaphoid rotation

was observed to be higher without film when compared to with film, but all these rotations were very small.

Table 2.1 Kinematic results with and without film in the joint space

Bone	Transformation	With Film			Without Film		
		X (M-L)	Y (D-P)	Z (A-P)	X (M-L)	Y (D-P)	Z (A-P)
Lunate	*Translation*	1.29	0.88	-2.12	0.15	1.27	-1.77
	Rotation	-0.11	-0.13	-0.08	0.09	0.12	0.05
Scaphoid	*Translation*	0.56	1.36	-1.26	-0.06	1.22	-1.15
	Rotation	-0.05	-0.08	-0.02	0.02	0.10	0.04

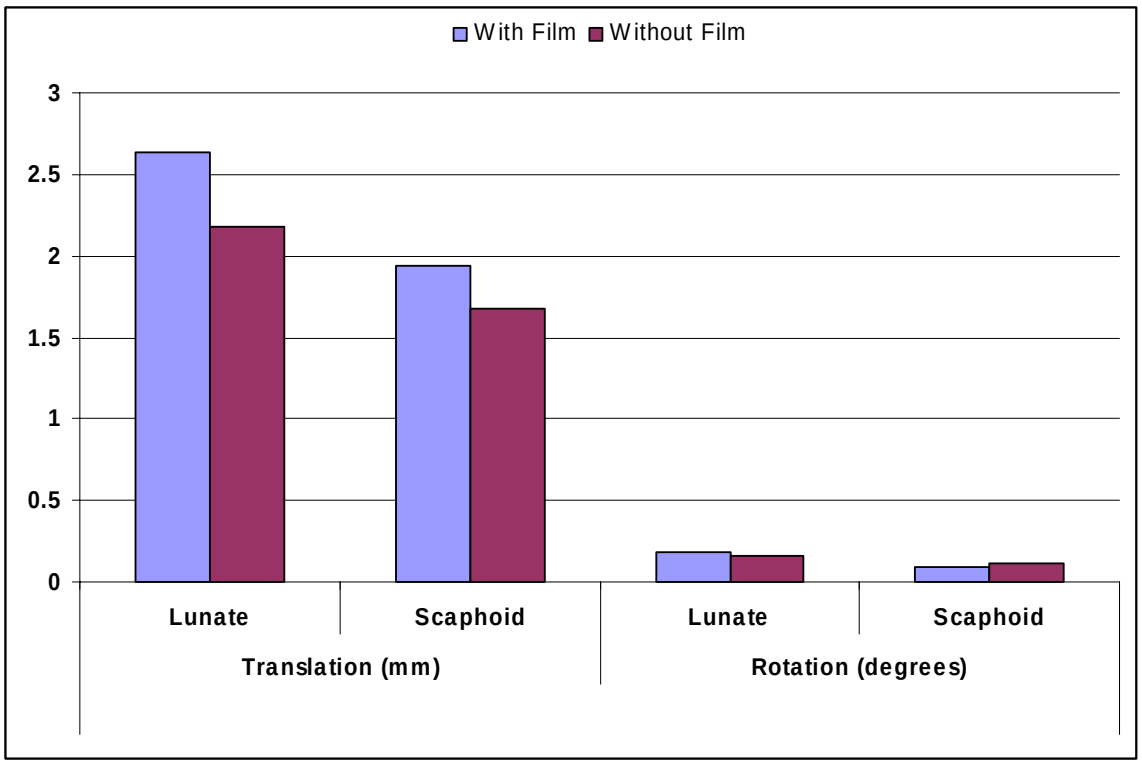

Figure 2.3 Magnitudes of carpal bone translations and rotations for models with and without film.

2.3.2. Contact Analysis

Table 2.2 Model results with and without film in the joint space

Measurement	Contact	With Film	Without Film
Force (N)	**RL**	99.71	23.80
	RS	57.52	71.97
Area (mm^2)	**RL**	64.41	32.63
	RS	60.09	57.08
Peak Pressure (MPa)	**RL**	1.98	2.42
	RS	2.69	1.49

Looking at model results obtained from contact analysis (Table 2.2), contact area measurements were consistently higher with the presence of film than without film. The average percent difference in radiolunate and radioscaphoid contact areas was found to be 51.3%. Radiolunate peak contact pressure with film was lower compared to without film while radioscaphoid peak pressure was higher with film compared to without film. The average percent difference in radiolunate and radioscaphoid peak contact pressures was found to be 31.2%. Radiolunate contact force was higher (by approximately 76 N) while radioscaphoid contact force was lower (by approximately 14 N) with the presence of film.

2.4. Discussion and Conclusion

Due to the widespread use of experimental methods such as pressure sensors to validate computational methods, it is important to understand the effects of film insertion into joint under investigation and take into account subsequent errors in contact mechanics that might arise as a result. As mentioned earlier, relative geometry and stiffness of sensor material when compared with articular cartilage can alter contact results significantly.

The primary cause of error produced by inserting a sensor into joint space is due to stiffness and thickness of film [8]. Films with lower stiffness values (relative to cartilage) are easier to deform and would therefore increase conformity between contact surfaces resulting in increased contact areas. The opposite is true as well. Stiffer films would decrease conformity due to reduced deformation thereby affecting articular surface contact, which might result in underestimation of contact areas. This could be a possible explanation for the 51.3% average error in radiolunate and radioscaphoid contact areas obtained from this study. This is a reasonable estimate as Liau et al have shown overestimation in contact area as high as 77% [9].

Models predicted average peak contact pressures to be 31.2% higher with film. Wu et al measured errors in joint contact pressures increased by 28% with film [8]. These findings are close to those obtained from this study, the problem being consistency of the current data. Peak contact pressure is highly dependant on geometry and kinematics and is the most difficult data to determine precisely. Joint_Model uses cartilage thickness as one factor to determine contact pressure distribution. Presence of film in joint space alters cartilage geometry from a modeling perspective. Also, results have shown presence of film to alter contact kinematics. Both geometry and kinematics could possibly explain the error in contact pressure measurements.

Errors in maximum shear stress due to presence of film while relatively low (less than 10%), have been shown to occur [8]. Relative sliding and friction between film and cartilage surface can also be contributing factors leading to errors when using Fuji-

scale film. Presence of film could possibly explain the higher kinematics (especially lunate and scaphoid translations) obtained with the presence of film for this study.

Based on the results obtained with the presence of film in the radiocarpal joint space, the stated hypothesis was partially fulfilled. Radiolunate and radioscaphoid contact areas were higher with the presence of film while only radioscaphoid peak contact pressure was higher. On the other hand, average radiocarpal peak contact pressure was higher with film than without.

This study showed that presence of film in joint space does indeed cause an alteration in radiocarpal kinematics and contact characteristics. This has to be taken into consideration for future *in vitro* studies requiring experimental measurements using pressure sensors. The main limitation to this study was the analysis of a single specimen only. In future, testing of multiple specimens is required to establish significant differences in kinematics and contact characteristics resulting from insertion of film in radiocarpal joint space.

2.5. References

1. Anderson DD, Daniel TE. A contact-coupled finite element analysis of the radiocarpal joint. Semin Arthroplasty 1995;6(1):30-6.
2. Anderson DD, Goldsworthy JK, Li W, James Rudert M, Tochigi Y, Brown TD. Physical validation of a patient-specific contact finite element model of the ankle. J Biomech 2007;40(8):1662-9.
3. Harris ML, Morberg P, Bruce WJ, Walsh WR. An improved method for measuring tibiofemoral contact areas in total knee arthroplasty: a comparison of K-scan sensor and Fuji film. J Biomech 1999;32(9):951-8.
4. Kazuki K, Kusunoki M, Shimazu A. Pressure distribution in the radiocarpal joint measured with a densitometer designed for pressure-sensitive film. J Hand Surg [Am] 1991;16(3):401-8.
5. Martinelli L, Hurschler C, Rosenbaum D. Comparison of capacitive versus resistive joint contact stress sensors. Clin Orthop Relat Res 2006;447:214-20.
6. Wilson DC, Niosi CA, Zhu QA, Oxland TR, Wilson DR. Accuracy and repeatability of a new method for measuring facet loads in the lumbar spine. J Biomech 2006;39(2):348-53.
7. Wilson DR, Apreleva MV, Eichler MJ, Harrold FR. Accuracy and repeatability of a pressure measurement system in the patellofemoral joint. J Biomech 2003;36(12):1909-15.
8. Wu JZ, Herzog W, Epstein M. Effects of inserting a pressensor film into articular joints on the actual contact mechanics. J Biomech Eng 1998;120(5):655-9.

9. Liau JJ, Hu CC, Cheng CK, Huang CH, Lo WH. The influence of inserting a fuji pressure sensitive film between the tibiofemoral joint of knee prosthesis on actual contact characteristics. Clin Biomech 2001;16(2):160-6.
10. Liau JJ, Cheng CK, Huang CH, Lo WH. Effect of fuji pressure sensitive film on actual contact characteristics of artificial tibiofemoral joint. Clin Biomech 2002;17(9-10):698-704.
11. Waller AJ. Master's Thesis: Refinement and validation of MRI-based models for joint contact mechanics. Mechanical Engineering, University of Kansas, 2007.
12. Woltring HJ. 3-D attitude representation of human joints: a standardization proposal. J Biomech 1994;27(12):1399-414.
13. Kwak SD, Blankevoort L, Ateshian GA. A Mathematical Formulation for 3D Quasi-Static Multibody Models of Diarthrodial Joints. Comput Methods Biomech Biomed Engin 2000;3(1):41-64.

3. Validation Study

3.1. Background

Degenerative joint disease is a major ailment affecting substantial portion of the population over 50 years of age [1]. This stresses the importance of developing cost effective tools for detection and prevention of arthritis. The underlying cause of Osteoarthritis (OA), which is the most predominant form of arthritis, is relatively unknown, as is the cause of the variation in rate of progression between subjects. The implementation of patient specific tools is currently under investigation, with an emphasis on computational models. Computational modeling is a cutting edge investigative technique that simulates *in vivo* mechanics and is useful for joint contact analysis. Further development in this area will provide insight into novel ways of diagnosis and preventive measures against osteoarthritis.

Several techniques exist for joint contact analysis using computational models. One method is rigid body spring modeling (RBSM). These models provide an accurate description of bone geometry. RBSM uses a set of finite compression springs to represent articular surface [2-8] and ligaments and tendons are modeled as tension springs. Cartilage material properties of interest are used to define spring properties and depending on analysis, can be simulated on one or both contact surfaces. This technique is relatively easy to implement and computationally efficient when compared to finite element (FE) models.

Another technique is finite element modeling (FEM). With evolution of computational power, development and analysis of complex 3D solid models is now

possible [9-17], thereby increasing the popularity of this technique. Using CT or MR scans to obtain geometric information, highly accurate models can be constructed. In most instances when using CT scans, cartilage geometry is uniformly projected from bone surface [18-24]. On the other hand, MR scans can be used to construct complete models, with regions of bone and cartilage directly defined from the images. Models are generated by meshing finite elements and accuracy depends on geometric data, material properties, mesh definition and boundary conditions [25-28]. The higher the model complexity, the more time-consuming the FE process and in many cases, there is a compromise between computational time and accuracy of solution.

A third technique is multi body contact modeling. In this technique, 3D surface models are generated from MR images. The surfaces include the outer boundary of the bones, whether actually cartilage or bone. Images for model construction are generally obtained in a relaxed configuration in order to avoid initial deformation. The position of interest is obtained by kinematics application (from a loaded MRI, for instance) or from application of loading conditions. Solutions are determined from interpenetration of contact surfaces [29,30] and solved to satisfy the boundary conditions. Several multi-body contact programs exist, namely DADS, ADAMS, DYNAMAN, Working Model, Articulated Total Body Model etc. Contact modeling is computationally efficient compared to FEM and has more flexible contact rules and hence forms the basis of this study. Following studies have shown the effectiveness of this method and justified its use for contact analysis.

Radiocarpal contact mechanics were investigated using contact modeling [30]. MR scans of the wrist of four human subjects were acquired in both unloaded (relaxed) and loaded (light grasp) configurations using a 1.5 Tesla whole body MRI scanner. Three dimensional surface models of the radius, lunate and scaphoid were constructed from relaxed images. Kinematic transformations were obtained by surface registration from unloaded to loaded configuration and these were applied to the models. Radioscaphoid, radiolunate and scapholunate articulations were analyzed using Joint_Model program. While results were promising, study was subject to limitations such as low image resolution and signal-to-noise (SNR) ratio, low geometric accuracy due to thick slices low precision in registration, and lack of model validation.

In a related study to validate the technique [31], a 9.4 Tesla MRI scanner was used to obtain high resolution and SNR images (both relaxed and simulated light grasp) of three cadaver forearm specimens. Slice thickness was reduced from 2 mm [30] to 1 mm. Models of the radius and carpal bones under investigation were constructed from relaxed image sets. A more precise registration method based on 3D voxel normalized mutual information was used to obtain kinematic transformations from the unloaded to loaded state. These kinematics parameters were implemented in the Joint_Model program for contact analysis. Experimental data was collected for comparison with model results. Peak pressures were within expected values and contact intensity and location matched experimental and model results. Also, direct contact area measurements from MR scans matched closely with model results.

This technique was further refined by prior validation work in our lab [32]. Five cadaver forearm specimens were analyzed for radiocarpal contact mechanics which were compared with experimental data. Five wrist tendons (3 flexors and 2 extensors) were isolated for joint loading that simulated light grasp (as opposed to three [31] to improve joint stability). Both relaxed and grasp images were acquired using a 9.4 Tesla MRI scanner. Three dimensional surface models were constructed from relaxed MR images. A 3D voxel registration technique was used to determine motion from the unloaded to loaded configuration. Contact area results obtained from models were very similar to direct contact area measurements from MR images. Contact forces were similar to Tekscan sensor measurements. Peak pressures were similar to Pressurex Fuji-scale film measurements. That study further demonstrated the feasibility of using MRI-based contact modeling for joint contact analysis. However, the scanner used to obtain images was not feasible for human subjects.

In order to apply computational models for evaluation of *in vivo* joint contact mechanics, it is necessary to demonstrate that the chosen modeling strategy is able to make necessary predictions to a certain degree of accuracy, hence the need for validation. In the past, different techniques have been used for validation including comparison with published work or with corroborative results from other analytical methods [33]. While these methods serve to establish some general level of confidence, a more definitive validation can be provided by comparison with direct experimental measures [33]. Several studies have used in situ experimental data to validate computational models [34-36]. Often, validation is based on how closely the

experimental and model data agree. Anderson et al. validated patient-specific contact FE models using a high resolution pressure sensor [33]. Contact stress distributions were compared between experimental and computational results. Validation was based on direct comparison with physical measurements from corresponding cadaver loading tests. The contact stress and contact area comparisons were reasonable while pixel-by-pixel comparisons of stress distribution across articular surface showed considerable agreement. Papaioannou et al. used biplane dynamic Roentgen stereogrammetric analysis (DRSA) coupled with Tekscan sensor to validate specimen-specific knee joint FE models [37]. Convergence of FE solution indicated accuracy while confidence in model validity itself was achieved by comparison of contact variables with direct experimental measures. Models were found to predict most of the contact variables measured experimentally. Anderson et al. conducted a study to validate a finite element model to predict cartilage contact pressure in the human hip joint [38]. The model was considered validated as the FE predictions compared favorably with experimental measurements and published experimental data. Validation criteria vary, and many studies fail to state a quantitative criterion. One criterion for validation is an average model error of less than two times the accuracy/repeatability of the experimental measure for comparison. Based on this approach and results of experimental accuracy studies conducted in our lab [32], 20% error was selected for contact force validation and 25% error was selected for peak contact pressure validation. Contact area measurement is less-well quantified but is consistently better than force so 15% error

was selected for contact area validation and this was chosen as the primary validation criterion.

The purpose of this study was to validate MRI-based modeling of functional loading in a 3 Tesla clinical MRI scanner. Protocols matched those planned for future evaluation of *in vivo* joint mechanics. The final objective of all the *in vitro* studies conducted thus far is to have a means of evaluating *in vivo* joint mechanics to determine the effects of injury and the efficacy of surgical repair/reconstruction, and to provide insight into pathomechancis leading to joint degeneration. This validation study is necessary before moving to *in vivo* clinical testing.

3.2. Methodology

3.2.1. Specimen Preparation

Three cadaver forearms specimens were used for this study. Dissection involved two key stages, firstly isolation of bones and tendons of concern and secondly, volar dissection of the radiocarpal joint capsule.

Previous studies [31] performed isolation of the flexor digitorum superficialis (FDS), the flexor digitorum profundus (FDP) and the flexor pollicis longus (FPL) tendons only and this lead to the need to secure the hand to prevent wrist flexion. Subsequently a different approach was used [32] by also isolating two extensors; extensor carpi ulnaris (ECU) and extensor carpi radialis (ECR). This provided more natural joint stability and prevention of wrist flexion during the simulation of light grasp. This augmented approach was used for this study (Fig. 3.1).

Figure 3.1 Isolation of wrist extensors (A) and flexors (B) for joint loading.

Due to similar function, the extensor carpi radialis longus and extensor carpi radialis brevis were sutured together to form a single ECR tendon unit. Once isolation was completed, tendons were wrapped in saline soaked gauze to prevent drying and loss of function. Saline was periodically sprayed on the tendons to prevent them from drying. Suture loops were attached to all isolated tendons to allow tensile loading.

Soft tissue was removed along a 10 cm length of the forearm, 2 cm proximal to the joint and moving proximal to expose the radius and ulna. Care was taken to leave the interosseous membrane intact as studies have shown it to play a role in wrist joint

stability [39]. Two 6.35 mm holes were drilled through the radius and one through the ulna to attach the specimen to a base plate using plastic bolts (Fig. 3.2). It was ensured that the holes were aligned to maintain forearm neutral rotation for the duration of testing and imaging.

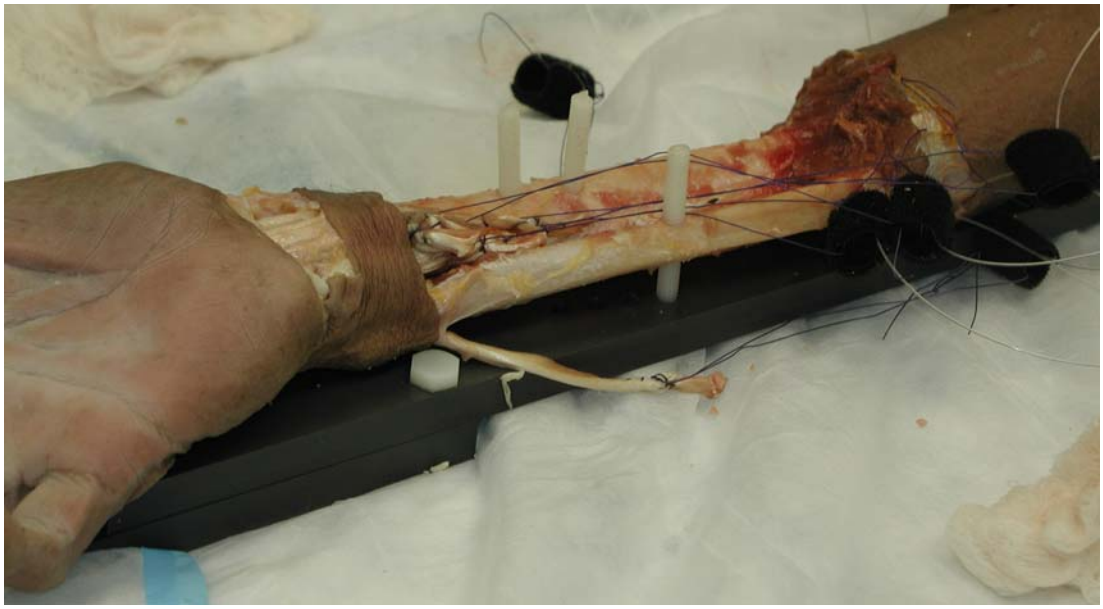

Figure 3.2 Attachment of specimen to base plate. Sutured loops and nylon line connections also shown.

3.2.2. Experimental Setup

In order to be compatible with the MRI scanner, only non-ferrous materials were used in the experimental setup. The test rig along with side components were fabricated entirely from plastic. The pulley system was attached to the stand which provided a stable platform for joint loading. Connecting plates (3 × 0.5 inches) of variable lengths were used to interconnect the base plate and loading stand depending on the desired placement within the MRI scanner (Fig. 3.3). This setup allowed for consistent joint loading and precise center positioning in the imaging space. Static

load was applied using water jugs, pre-filled and weighed for a known load, and connected with the help of a pulley system to the tendons via 40 lb (178 N) nylon lines.

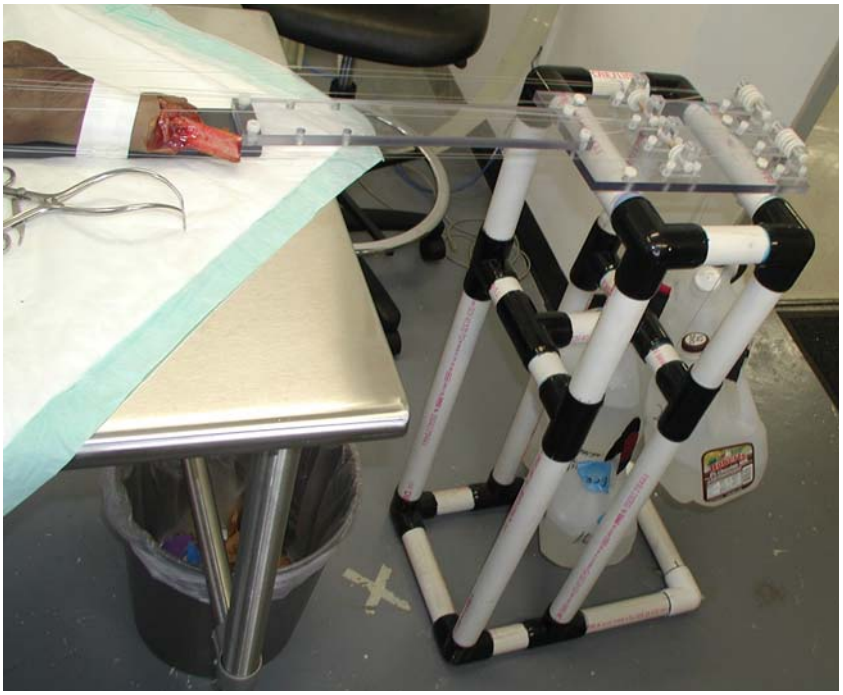

Figure 3.3 Experimental setup showing stand, pulley system and connecting plates.

A total of 110 N was applied to the joint to simulate light grasp [32]. Weight distribution across tendons was based on resisting wrist flexion and on loads proportional to respective muscle cross-sectional area. During experimental and imaging data acquisition, 30 N was applied to both ECU and ECR, 20 N to both FDP and FDS while the FPL was loaded with 10 N (Fig. 3.4). Before load application, a cylindrical PVC pipe (1.5 inch outer diameter) was placed in the hand as an object for simulated grasp. Fingers were taped around the pipe to maintain position without

tendon loads. To maintain wrist stability extensors were loaded first, followed by the flexors.

Figure 3.4 Experimental setup showing mechanism for joint loading.

3.2.3. Experimental Pressure Measurements

Several techniques have been proposed to measure in situ joint contact forces and pressures. This study made use of pressure sensitive film and an electronic pressure sensor for experimental measurements.

3.2.3.1. Pressure Sensitive Film

This study used Pressurex® Fuji-scale film (Sensor Products Inc., East Hanover, NJ). Pressurex is a high resolution film that comprises a transfer and a developer sheet which releases color dye proportional to the applied pressure. This study used Super Low type Pressurex film with a maximum thickness of 0.008 in (0.2 mm

approximately) which was reasonably able to conform to curved surfaces, making it appropriate for biomechanical applications. Pressure variation across film was interpreted using a custom calibration routine.

The system was calibrated under controlled conditions immediately prior to specimen testing in order to minimize environmental effects on film performance. Calibration was performed using a custom fixture in an Instron Materials Testing Machine (Model #8511, Instron Corp., Canton, MA). The fixture comprised a flat ended cylindrical indenter 0.625 in (15.875 mm) diameter and a flat base both lined with a layer of shore 80A rubber 1.6 mm thick. The rubber was chosen based on modulus similar to human articular cartilage. Film was placed between the indenter and base and loads applied from 100 to 1000 N in 100 N increments and held for 30 seconds each. The intensity profiles were scanned at 72 dpi resolution and saved as image files for calibration analysis (Fig. 3.5).

Figure 3.5 Sample calibration data (Specimen 3) from Pressurex sensor.

For this study, a code written in MATLAB (Mathworks Inc., Natick, MA) based on pixel-by-pixel analysis was used to analyze image color intensity. 3D arrays of red, green and blue values for individual pixels were obtained for each calibration image. Normalized red values for each pixel were determined from ratio of red value to total intensity (sum of red, green and blue values). Similarly, normalized blue

values were also determined. The calibration curve was a function of difference between normalized red and normalized blue values and the applied pressure (determined from known applied force and area) [32]. A cubic equation was fit to the data obtained and was used to calculate contact pressures from specimen testing (Fig. 3.6).

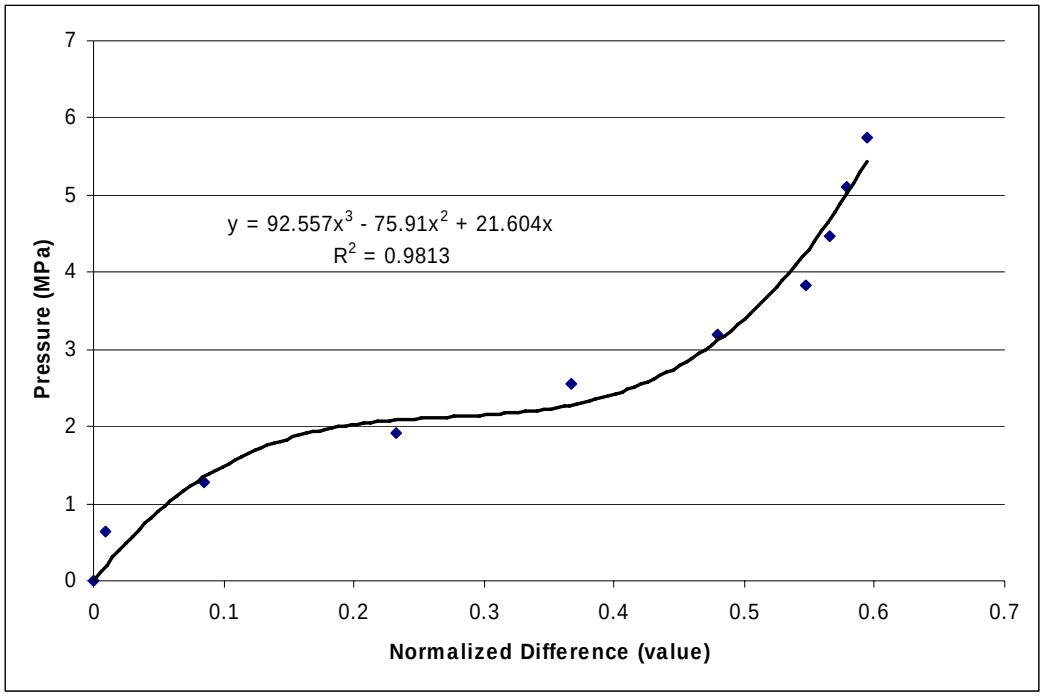

Figure 3.6 Sample calibration curve (Specimen 3) showing cubic regression equation and correlation coefficient.

Figure 3.7 Sample template (Specimen 3) showing radioscaphoid (left) and radiolunate (right) contact intensity profiles.

For testing, specific film templates were created to match the two fossa on the radius, along with a volar tab to facilitate insertion and extraction without interfering with results (Fig. 3.7). Use of templates reduced crimping of film during insertion, loading or extraction. Care was taken to cover the templates in a thin layer of plastic wrap to protect from damage and reduced performance due to the presence of synovial fluid and saline solution. The template was inserted into the radiocarpal joint and the joint subsequently loaded in simulated grasp as described earlier. Loads were applied for approximately 30 seconds to obtain a satisfactory profile and five trials conducted for each specimen. Similar analysis as calibration was performed and pixel-by-pixel contact pressure distributions obtained from the intensity profiles using the cubic calibration relation. Contact areas and forces were also determined.

3.2.3.2. Electronic Pressure Sensor

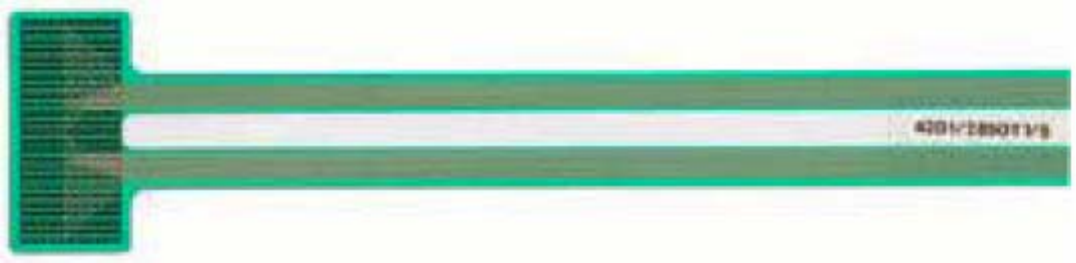

Figure 3.8 Wrist Sensor Model #4201 used to acquire experimental data.

This study also used the K-Scan™ System (Tekscan Inc., South Boston, MA), Wrist Sensor #4201 (Fig. 3.8). This system is even more thin, flexible than Fuji-scale film and accurate in generating contact force, area and pressure measurements. Piezoresistive sensels convert changes in resistance due to applied loads into pressure measurement for each sensel. The sensor, electronic interface (handle) and software

(I-Scan) allow for real-time feedback and dynamic measurements. While the resolution of the Tekscan system is not as high as Pressurex film, dynamic response eliminates insertion/ extraction artifacts thereby improving the accuracy of results.

In order to fit within the radiocarpal joint space, the Wrist sensor was trimmed approximately 2 mm on both sides. Care was taken not to interrupt the central sensel grid and the sensor was resealed to maintain integrity. The Tekscan sensor was also calibrated under a series of known loads, and the output (Fig. 3.9) was saved for analysis.

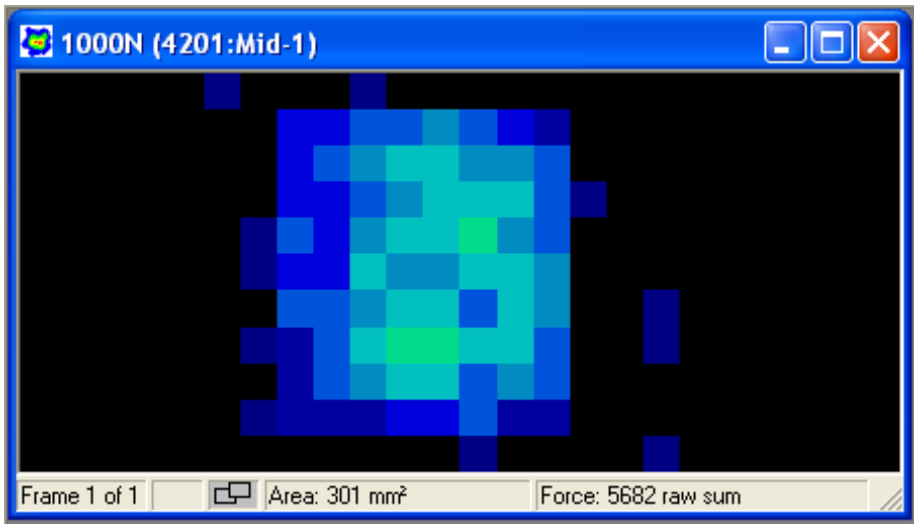

Figure 3.9 Sample calibration data (Specimen 3 – 1000N) from Tekscan sensor.

Applied pressures were related to average raw values determined from the sensels. Calibration data was fit to a quadratic curve for each sensor and used to calculate contact pressures from testing (Fig. 3.10). The experimental setup and procedures for acquiring Tekscan calibration and experimental data were similar to those previously described for Pressurex film. Three experimental measurement trials were conducted per specimen and the profiles were analyzed to obtain the results.

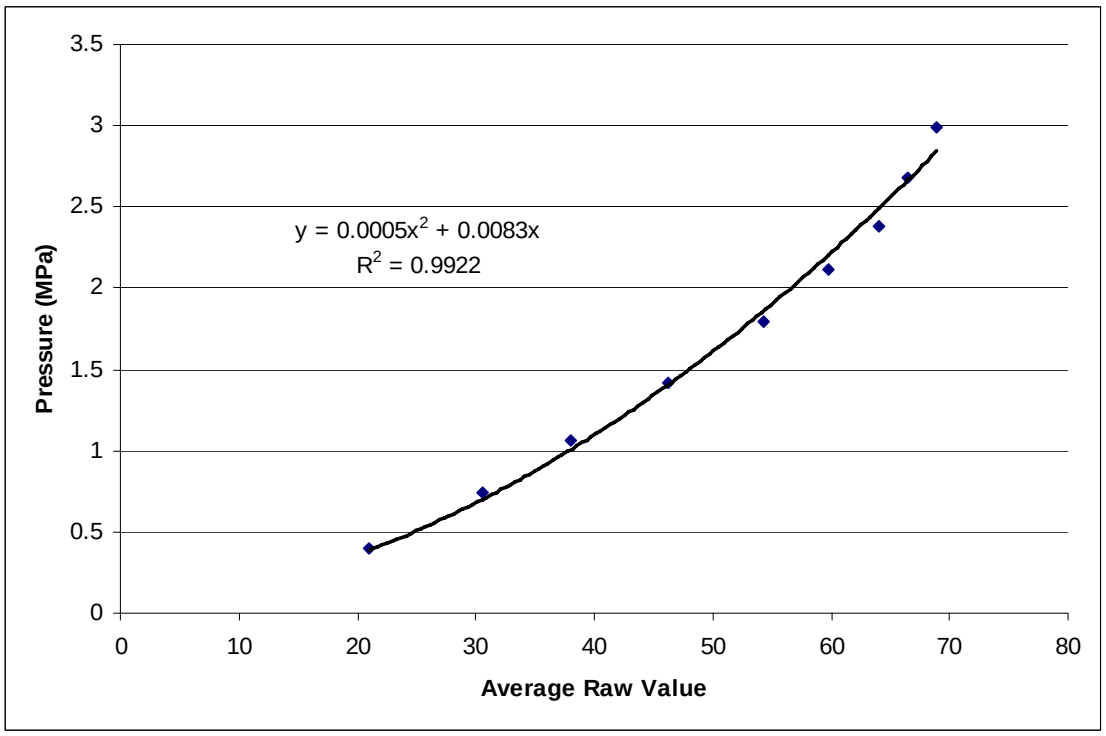

Figure 3.10 Sample calibration curve (Specimen 3) showing quadratic regression equation and correlation coefficient.

3.2.4. MR Data Acquisition

Anatomical geometry and kinematic boundary conditions for the models were obtained from MRI scans of the hand and wrist. These scans were performed using a 3 Tesla clinical MRI scanner (Siemens Allegra Systems, Siemens, USA). Frontal plane images were acquired during relaxed (unloaded) position and during simulated light active grasp (loaded configuration) using a constructive interference steady state (CISS) sequence and double loop custom surface coil.

For the unloaded configuration, scans were performed for a TR of 14.76 ms, TE of 7.38 ms, flip angle of 60°, averages (NEX) = 1, and partial phase and slice Fourier ratios of 6/8. The image sizes were 640 × 416 pixels with a 95 × 61.8 mm field of

view (FOV). The in-plane resolution was 0.15 mm with a slice thickness of 0.5 mm and 104 slices constituted the volume. For the loaded configuration, scans were performed for a TR of 11.98 ms, TE of 5.99 ms, flip angle of 60°, averages (NEX) = 1, and partial phase and slice Fourier ratios of 6/8. The image sizes were 320 × 208 pixels with a 95 × 61.8 mm FOV. The in-plane resolution was 0.3 mm (half that of unloaded) with a slice thickness of 1 mm and 52 slices constituted the volume. The lower resolution images reduced scan time (to 196 seconds) consistent with planned *in vivo* studies with active grasp scans. Relaxed images maximized resolution for accurate undeformed model geometry (Fig. 3.11).

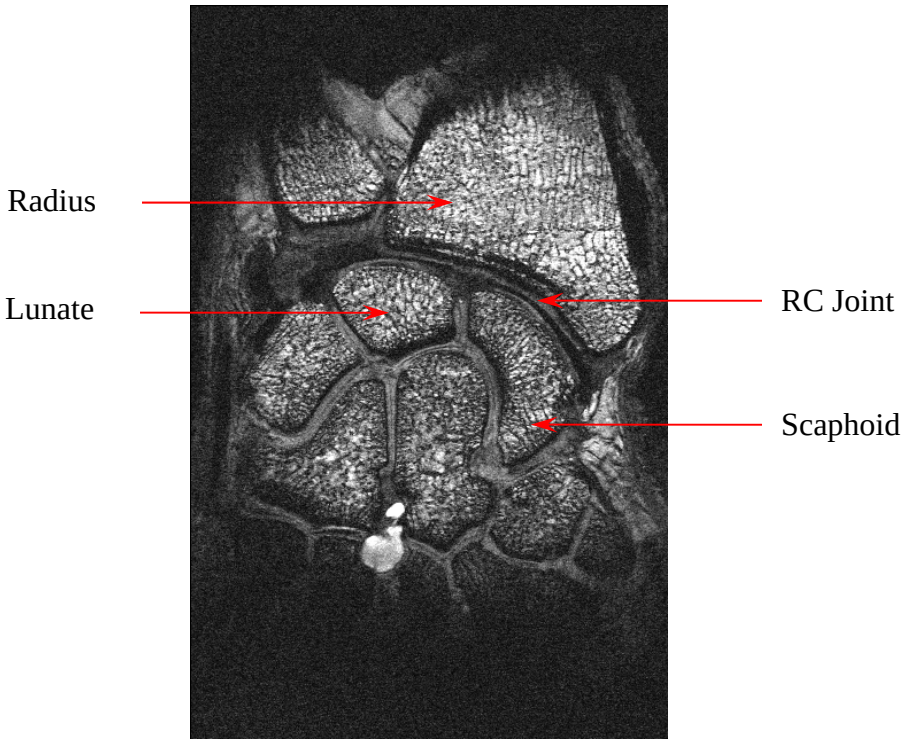

Figure 3.11 Sample MR image (Specimen 3) showing radiocarpal (RC) joint in unloaded configuration.

3.2.5. Segmentation and Model Construction

Manual segmentation of radius and carpal bones (and their respective cartilage surfaces) for surface models was performed using custom in-house software MPXImage (Ted Manson, University of Pittsburgh, 1998).

Figure 3.12 Anchor (yellow) and control (green) points forming Bezier curve.

Bezier splines were superposed on images and adjusted through multiple anchor and control points to fit the outer contour of the bone with cartilage (Fig. 3.12). Points on the contours were not restricted to pixel centers, resulting in smooth primary contours. In order to determine quality and accuracy of segmentation, contours were imported into PED software (Damion Shelton, University of Pittsburgh 2000) (Fig. 3.13). PED assembles multiple contours in 3D and allows for evaluating contours for anomalies, and identify segmentations that may need to be double-checked.

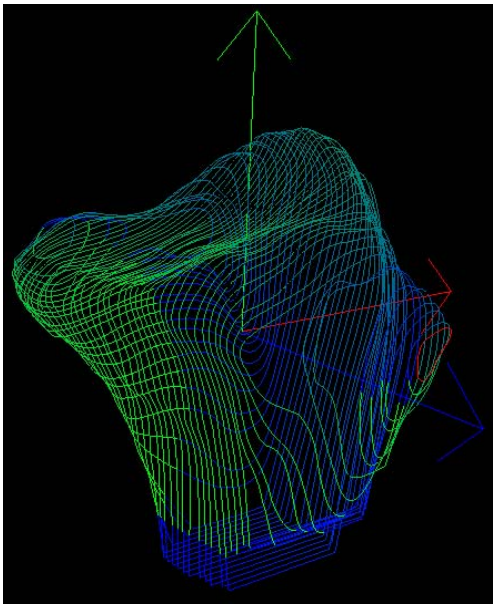

Figure 3.13 3D point cloud (Specimen 3 Radius) of segmented contours in PED.

Geomagic Studio 9 (Raindrop Geomagic, Research Triangle Park, NC) was used to construct 3D surface models of the unloaded bones (Fig. 3.14). Text files containing coordinates of bone contours were imported into Geomagic. The total number of points constituting 3D carpal bone geometry was reduced, in order to make file size compatible with contact analysis software, and surface wrap of points generated. Since the unloaded images were scanned with 0.5 mm slice thickness, Z values were scaled to obtain anatomically precise models. The surface geometry models of carpal bones from Geomagic were then converted to a format compatible with the Joint_Model program.

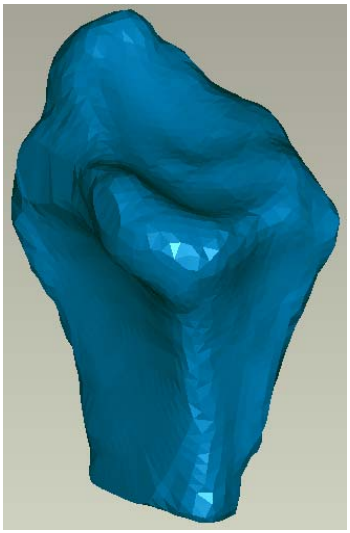

Figure 3.14 3D surface model (Specimen 3 Radius) constructed from contour data.

3.2.6. Registration and Kinematic Analysis

In order to perform registration for kinematics boundary conditions, unloaded and loaded radius and carpal bones (without cartilage surfaces) were isolated from MRI scans (Fig. 3.15). Isolation was performed using Adobe Photoshop 6.0 (Adobe Systems Inc, San Jose, CA) software and the procedure involved deleting every detail, except the desired bone from each scan. Isolated cropped images (416 × 416 unloaded and 208 × 208 loaded) were saved for kinematic analysis.

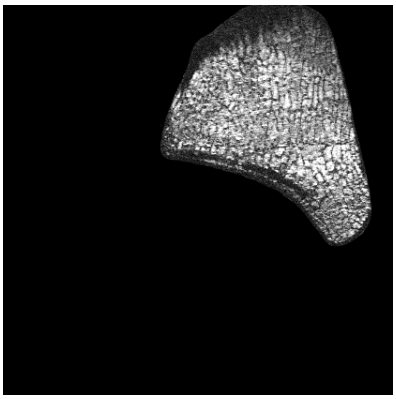

Figure 3.15 Isolation of cropped image (Specimen 3 Radius) for registration.

The basis of kinematic analysis was the assumption that bone tissue deforms negligibly during light grasp, while cartilage deforms even under the low loading. Analyze 5.0 (Analyze Direct, Lenexa, KS) was used to perform surface and/or volume registration. For this study, the radius was selected as reference (fixed) bone. Either surface or voxel registration methods were selected depending which was more accurate. Because volume registration does not always converge on the first trial, the procedure was repeated 25 times and all corresponding transformation matrices were saved for convergence analysis. This was achieved by comparing variation in magnitudes of translation vectors for each of the 25 transformations. If convergence was obtained, that transformation was used. If convergence was not obtained, either the last registration or the registration closest to the average translation vector was judiciously selected. The following 3D registration steps were performed for kinematic analysis.

The first step was to transform the loaded radius (reference bone) to the unloaded radius (that is the unloaded image coordinate system) and the resulting transformation matrices were saved. The most ideal transformation (determined from convergence analysis) was then used to transform the loaded carpal bones to the unloaded image coordinate system, and the resulting transformed image volumes were saved. Lastly, the unloaded carpal bones were transformed to match the loaded and transformed carpal bones (previously saved volume) to obtain the final kinematic transformation matrix. This kinematic transformation was converted to a translational vector and attitude (rotation) vector [8] as required by the Joint_Model program. The Analyze

left-handed coordinate system was accounted for by reversing signs of all translations and rotations.

Due to limitations in registration software, isolation of bone contours was performed on cropped images while models were inadvertently constructed from original uncropped images. This resulted in a change in location of the origin of the registration coordinate system with respect to the modeling coordinate system. The attitude vector starts at the origin and defines a single axis of rotation where magnitude of the vector is the rotation about the axis. Cropping of images caused a change in location of the origin of the images used for kinematics compared to the original images used to generate the bone models. Thus, translations associated with rotations would be slightly different in the two systems. These errors can be corrected based on known offsets from image cropping. For Specimen 1, cropping was done 130 pixels from the top and 94 pixels from the bottom of the image sets. For Specimen 2, cropping was done 100 pixels from the top and 124 pixels from the bottom and for Specimen 3, cropping was done 50 pixels from the top and 174 pixels from the bottom of the image sets. Based on the scale of rotations and centers of gravity of the carpal bones the errors were conservatively estimated to be less than 350 μm. For the analysis and data presented here, the kinematics were not recalculated. Using a consistent image set should be a priority when conducting future studies.

3.2.7. Contact Analysis

Contact analysis was performed using non-commercial Joint_Model program developed at University of Columbia (Kwak et al., Columbia University, 2000). The Joint_Model program considers 3D models as un-deformable and determines contact pressures from interpenetration of body surfaces with defined contact. Several key features make this program an effective modeling tool.

This software allows individual modification of bones, cartilage, ligaments and tendons and allows soft-tissue structure wrapping around bones along with 3D articular contact between bodies. Maximum overlap (penetration), contact pressures and pressure distribution (as a saturation map) along with peak contact pressure, contact forces and contact areas can all be displayed using this program and an output file allows examination of overlap or pressure at any model node. Finally, the program is computationally efficient when compared to other methods such as FEM.

Contact Pressure

The CTPSTRL Joint-Model program contact rule was used in this study. The fundamental principle of the CTPSTRL contact rule is that contact pressure is proportional to penetration at any point, as indicated by the equation $P = E\left(\frac{d}{t}\right)$, where P is the peak pressure, d is the local penetration (overlap), t is the total cartilage thickness for both bones and the ratio $\left(\frac{d}{t}\right)$ represents the approximate cartilage strain. Contact pressures are integrated over contact area to obtain contact force.

Contact Area

Calculation of contact area in Joint_Model program is based on area of complete and partial triangular surface facets involved in interpenetration. Area contribution for partially penetrating facets is based on the number of nodes penetrating and their penetration depth. The sum of areas from all facets with penetrating nodes gives the contact area.

The input for Joint_Model program was a data file containing two main definitions, BODY and CONTACT. The geometry and kinematics transformations (translations and rotations) for each carpal bone were defined under respective BODY definition. CONTACT defined the type and nature of contact between bodies. For this study CTPSTRL contact rule required material properties (modulus) of contact surfaces and total thickness of cartilage on both bones to be specified. Cartilage effective (relaxation) modulus of 4MPa and thickness of 2 mm (1mm each bone) were used for all bones as boundary conditions [29]. Kinematics (translation and attitude vectors from registration) were applied to the carpal bones by direct specification into input file. The analysis was displacement controlled. The program determined the solution for the specified boundary conditions and provided the output data for each defined bone contact pair.

3.2.8. Direct Contact Area Measurement

Contact areas were determined directly from MR images as an additional form of validation for measurements obtained from models. This is a straightforward procedure that can be used as *in vivo* verification of modeling accuracy.

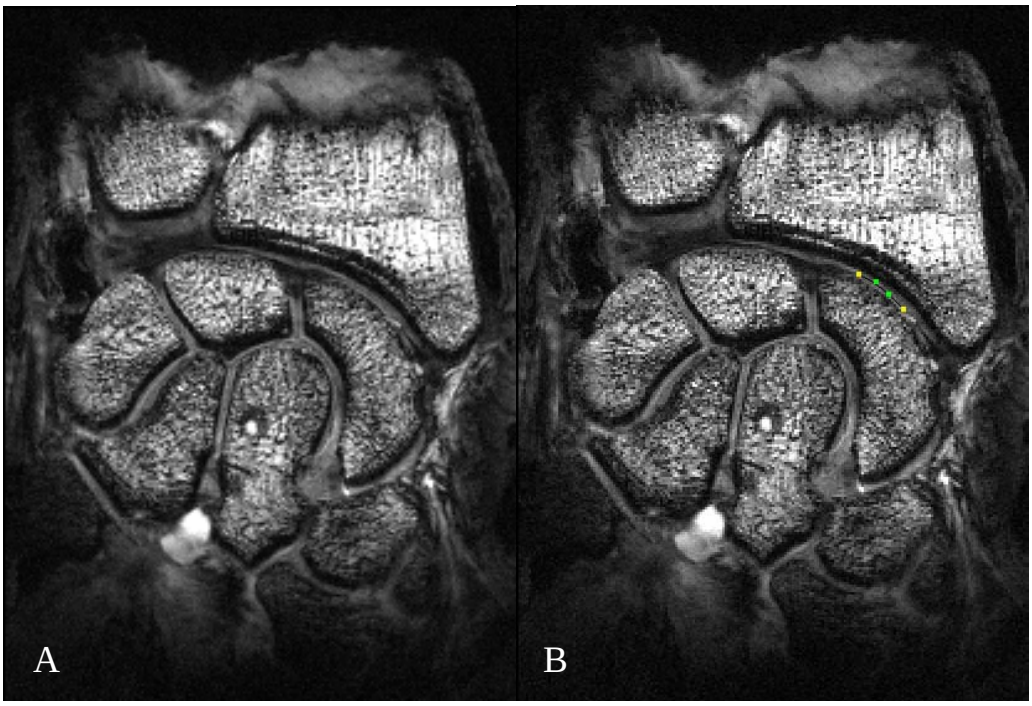

Figure 3.16 Loaded MR image showing (A) radioscaphoid contact and (B) segmented radioscaphoid contact (Specimen 3 – Slice 31).

Radiocarpal contact is visible in loaded MR configuration and was therefore segmented using MPXImage (similar procedure as model construction). Contour plot (arc) of contact region was defined for each contact pair and each image (Fig. 3.16) in the entire set. Contact arc lengths for each image were multiplied by slice thickness (to get effective area) and the areas from all images were added to determine total contact area for the pair.

3.3. Results

3.3.1. Kinematic Analysis

Table 3.1 Radiocarpal kinematics. Translation and rotation in mm and degrees respectively

Specimen	Bone	Transformation	X (M-L)	Y (D-P)	Z (A-P)
1	Lunate	*Translation*	-1.727	0.344	0.371
		Rotation	-0.500	-0.094	-0.056
	Scaphoid	*Translation*	-1.320	-1.284	0.069
		Rotation	-0.098	-0.152	0.014
2	Lunate	*Translation*	-1.361	0.560	0.233
		Rotation	-0.479	-0.174	-0.031
	Scaphoid	*Translation*	-1.332	-0.100	0.023
		Rotation	-0.305	-0.244	-0.046
3	Lunate	*Translation*	-0.110	0.587	0.480
		Rotation	-0.456	0.088	0.021
	Scaphoid	*Translation*	-0.102	0.455	0.381
		Rotation	-0.413	0.150	0.011

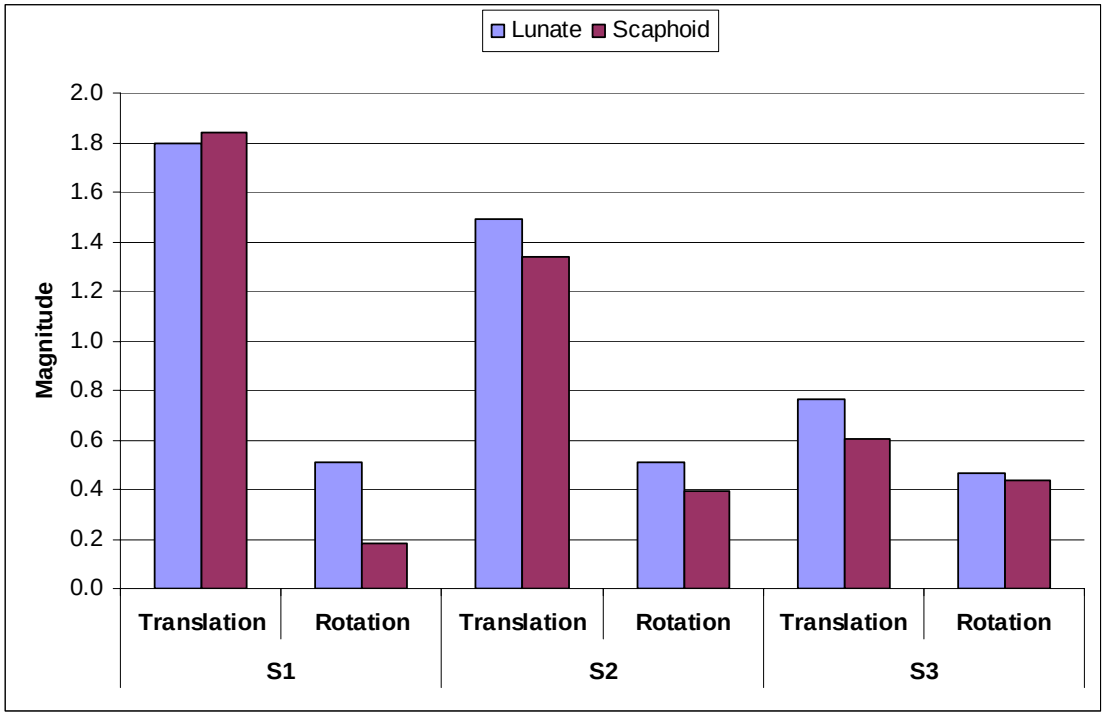

Figure 3.17 Showing magnitudes of translation and rotation for all specimens (S).

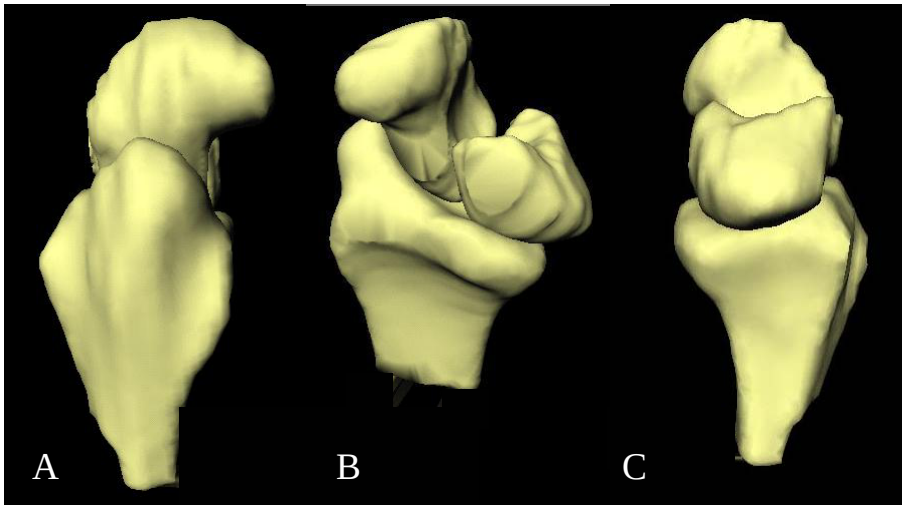

Figure 3.18 Specimen 3 radiocarpal contact model (A) lateral, (B) oblique and (C) medial views in Joint_Model.

Table 3.1 and Fig. 3.17 show kinematics obtained from registration for all specimens. Due to uniqueness in geometry and the positions during unloaded imaging, kinematics vary between specimens. Specimen 1 had the highest lunate and scaphoid translation magnitudes, that is, 1.799 mm and 1.843 mm respectively. Specimens 1 and 2 showed the highest lunate rotation (0.511 degrees) while Specimen 3 showed the highest scaphoid rotation (0.493 degrees). Except for Specimen 1 translation, the general trend was for higher lunate translations and rotations (magnitudes) when compared with scaphoid. The highest translations were in the medial-lateral direction except for Specimen 3 (highest in the proximal-distal direction). The highest rotations were about the medial axis. Overall, the transformations were characterized by very small (no greater than half degrees) rotations. Fig. 3.18 shows the radius and carpal bones in loaded configuration.

3.3.2. Contact Analysis

Table 3.2 shows experimental data for each trial collected using Tekscan sensor. Three trials were conducted and measurements were consistent amongst the trials. Averages of contact force, area and peak pressure for the three trials were taken for comparison with data acquired from models.

Table 3.2 Experimental data acquired using Tekscan sensor

Specimen	Contact	Measurement	Trial 1	Trial 2	Trial 3
1	RL	*Force (N)*	36.947	33.629	35.307
		Area (mm^2)	36.290	39.919	43.548
		Peak Pressure (MPa)	4.586	4.586	4.586
	RS	*Force (N)*	37.476	45.665	34.288
		Area (mm^2)	108.871	105.242	101.613
		Peak Pressure (MPa)	2.686	4.012	2.744
2	RL	*Force (N)*	18.364	14.121	13.141
		Area (mm^2)	116.129	105.242	105.242
		Peak Pressure (MPa)	1.034	1.034	0.977
	RS	*Force (N)*	29.497	21.918	20.711
		Area (mm^2)	61.693	50.806	43.548
		Peak Pressure (MPa)	2.829	1.408	1.581
3	RL	*Force (N)*	76.786	78.290	82.394
		Area (mm^2)	130.645	130.645	130.645
		Peak Pressure (MPa)	2.953	2.953	3.031
	RS	*Force (N)*	52.164	46.030	40.338
		Area (mm^2)	65.322	54.435	61.693
		Peak Pressure (MPa)	5.615	4.699	4.996

Table 3.3 shows the experimental data collected using Pressurex super low film. Contact forces, areas and peak pressures were interpreted from intensity profiles generated on templates (Fig. 3.7) during radiocarpal joint loading using calibration curves. Only peak pressure measurements were relatively close to the Tekscan and

model data. Contact force and area measurements were substantially underestimated (except for Specimen 2 forces). Due to these erratic results, Pressurex data was not used for validation.

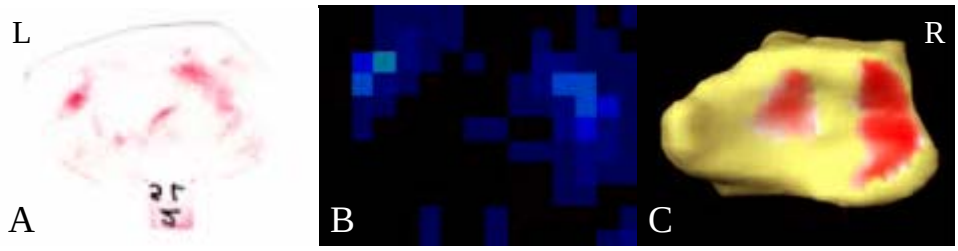

Figure 3.19 Specimen 3 intensity profiles (A) Pressurex, (B) Tekscan and (C) model for lunate (R) and scaphoid (L) contact.

Qualitatively, intensities were consistent between experimental and model measures (Fig. 3.19). Relative size and location of scaphoid and lunate contact on the radius correspond well. Results of this study are consistent with prior *in vivo* and experimental studies that indicate most of the contact to be in the dorsal region. This is evident from the contact intensities on the radius articular surface. Also, the general trend was for greater lunate contact intensities than scaphoid.

Table 3.3 Experimental, model and direct measurements

Specimen	Contact	Measurement	Pressurex	Tekscan	Model	Direct
1	RL	*Force (N)*	10.124	35.294	20.736	
		Area (mm^2)	7.331	39.919	49.182	43.369
		Peak Pressure (MPa)	3.044	4.586	0.975	
	RS	*Force (N)*	22.925	39.143	187.130	
		Area (mm^2)	15.532	105.242	103.900	89.947
		Peak Pressure (MPa)	2.362	3.147	2.976	
2	RL	*Force (N)*	29.643	15.209	13.298	
		Area (mm^2)	11.059	108.871	58.295	100.162
		Peak Pressure (MPa)	3.001	1.015	0.881	
	RS	*Force (N)*	43.877	24.042	58.588	
		Area (mm^2)	12.923	52.016	69.258	55.863
		Peak Pressure (MPa)	4.633	1.939	1.739	
3	RL	*Force (N)*	30.387	79.156	94.067	
		Area (mm^2)	18.141	130.645	110.771	124.845
		Peak Pressure (MPa)	2.253	2.979	1.432	
	RS	*Force (N)*	20.282	46.177	32.091	
		Area (mm^2)	13.420	60.484	65.768	63.410
		Peak Pressure (MPa)	1.996	5.103	0.998	

Table 3.3 shows a summary of all experimental, model and directly image measured data. Looking at contact forces for all specimens (Fig. 3.20), Tekscan and model results matched reasonably well. The general trend was for both Tekscan and model to predict lower radiolunate contact forces compared to radioscaphoid contact forces. Comparing Tekscan and model data, for Specimens 1 and 2, Tekscan predicted higher radiolunate contact forces (35.294 and 15.209 N respectively) than the MRI-based model (data). On the other hand, model predicted higher radioscaphoid contact forces compared to Tekscan data. Model results were high for Specimen 1 and Specimen 2 radioscaphoid contact forces. The 187.13 N

radioscaphoid contact force for Specimen 1 is unreasonable and must be the result of compounded errors. For Specimen 3, the model predicted higher radiolunate contact force compared to Tekscan data and Tekscan predicted higher radioscaphoid contact force compared to model data.

Comparing contact area results between Tekscan, model and direct measurements (Fig. 3.21) it was observed that the three matched closely for Specimens 1 and 3. In case of Specimen 2, model underestimated radiolunate contact area and somewhat overestimated radioscaphoid contact area compared to Tekscan and direct measurements. Tekscan and direct measurements matched closely for all specimens. Considering radiolunate contact areas, the model registered highest value for Specimen 1 (49.182 mm^2), while Tekscan data was the highest for Specimens 2 and 3 (108.871 and 130.645 mm^2 respectively). Looking at radioscaphoid contact areas, Tekscan registered highest value for Specimen 1 (105.242 mm^2), while model data was highest for Specimens 2 and 3 (69.258 and 65.768 mm^2 respectively).

Comparing peak pressures between Tekscan and model data (Fig, 3.22), results obtained were inconsistent. Looking at Specimen 1, Tekscan and model radioscaphoid peak contact pressures closely matched. For Specimen 2, both radiolunate and radioscaphoid peak contact pressures closely matched between Tekscan and model results. On the other hand, Tekscan measured high radiolunate peak contact pressure for Specimen 1. Tekscan results were also high for Specimen 3 radiolunate and radioscaphoid peak contact pressures. The general trend was for

Tekscan to measure higher peak contact pressure values than were found using the model.

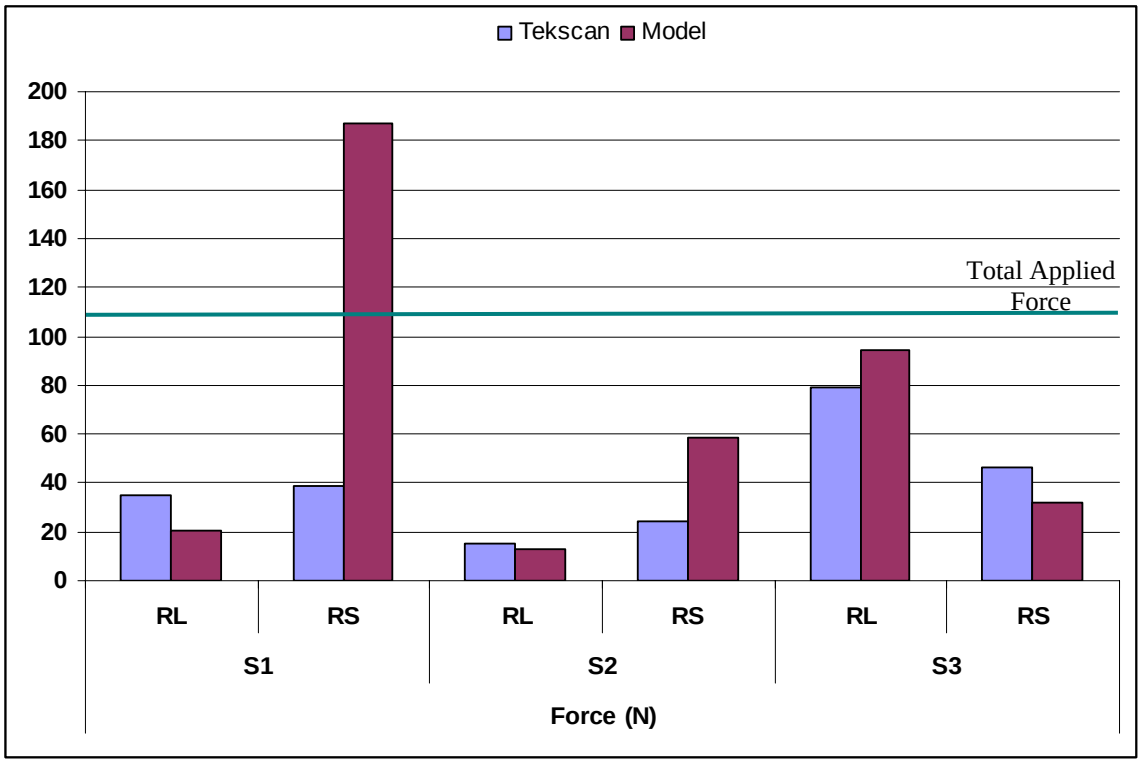

Figure 3.20 Radiolunate (RL) and radioscaphoid (RS) contact force for all specimens (Specimen 1: S1; Specimen 2: S2; Specimen 3: S3).

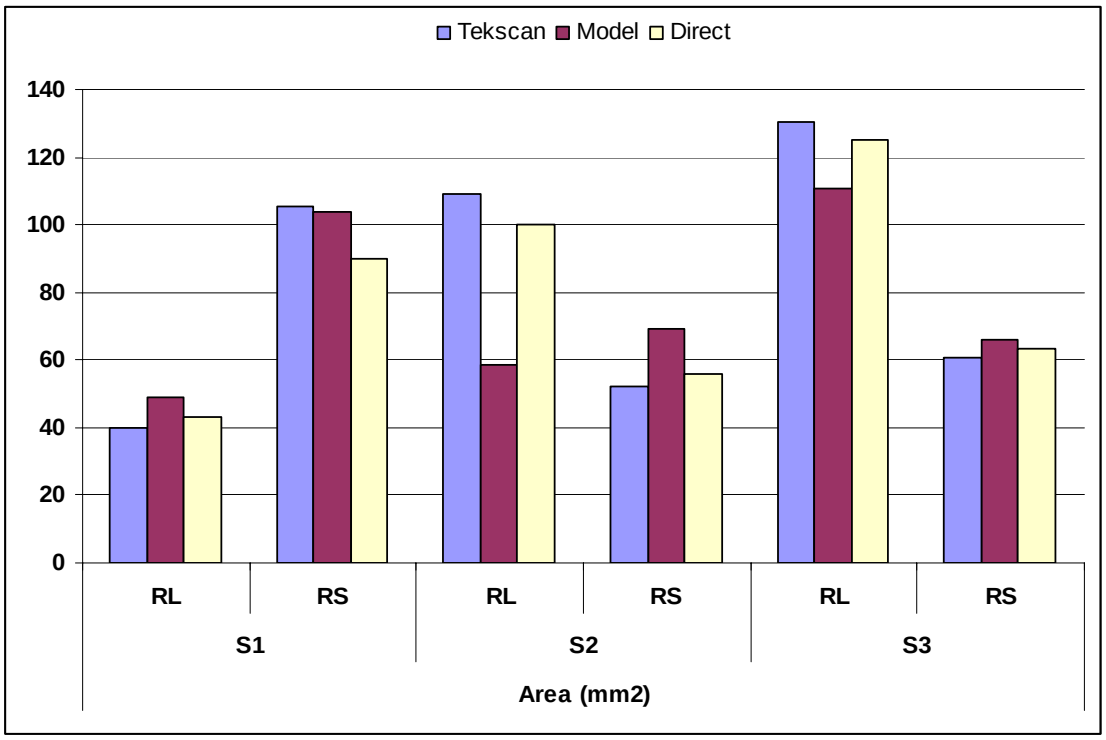

Figure 3.21 Radiolunate (RL) and radioscaphoid (RS) contact area for all specimens.

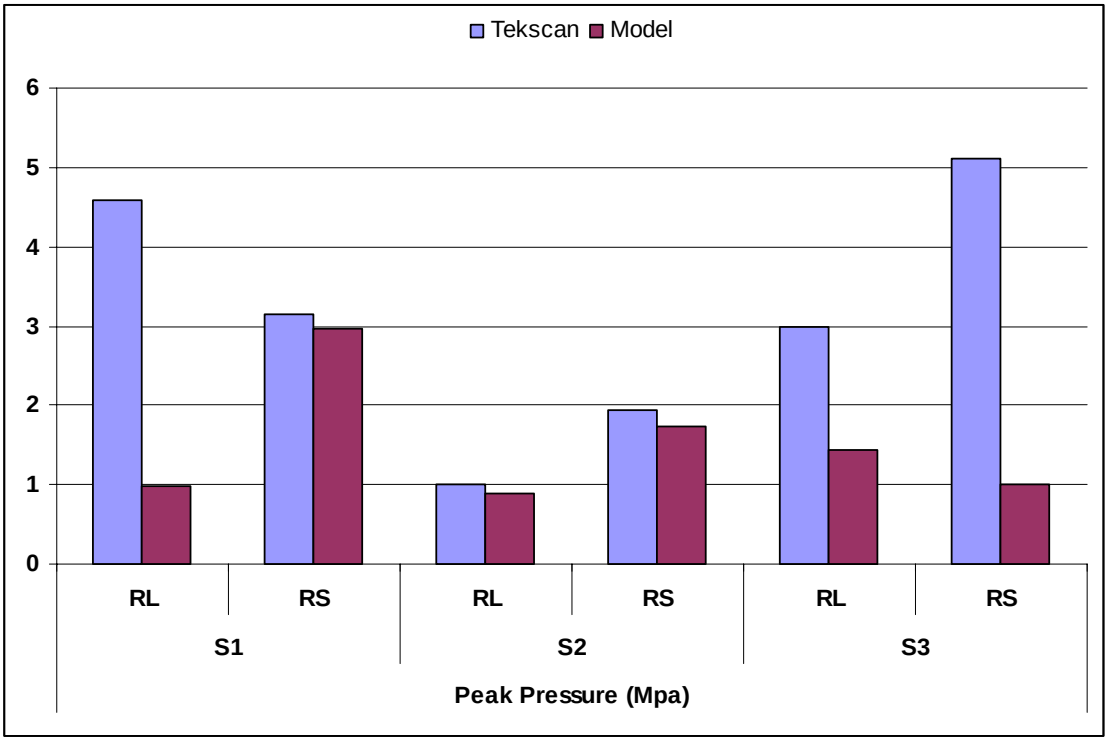

Figure 3.22 Radiolunate and radioscaphoid peak contact pressure for all specimens.

Table 3.4 Comparison of experimental and model force measurements

Force (N)					
Specimen	**Contact**	**Tekscan**	**Model**	**% Difference**	**Avg % Difference**
1	**RL**	35.294	20.736	41.2	209.7
	RS	39.143	187.130	378.1	
2	**RL**	15.209	13.298	12.6	78.1
	RS	24.042	58.588	143.7	
3	**RL**	79.156	94.067	18.8	24.7
	RS	46.177	32.091	30.5	

Table 3.5 Comparison of experimental and direct MR area measurements

Area (mm^2)					
Specimen	**Contact**	**Tekscan**	**Direct**	**% Difference**	**Avg % Difference**
1	**RL**	39.919	43.369	8.6	11.6
	RS	105.242	89.947	14.5	
2	**RL**	108.871	100.162	8.0	7.7
	RS	52.016	55.863	7.4	
3	**RL**	130.645	124.845	4.4	4.6
	RS	60.484	63.410	4.8	

Table 3.6 Comparison of experimental and model area measurements

Area (mm^2)					
Specimen	**Contact**	**Tekscan**	**Model**	**% Difference**	**Avg % Difference**
1	**RL**	39.919	49.182	23.2	12.2
	RS	105.242	103.900	1.3	
2	**RL**	108.871	58.295	46.5	39.8
	RS	52.016	69.258	33.1	
3	**RL**	130.645	110.771	15.2	12.0
	RS	60.484	65.768	8.7	

Table 3.7 Comparison of direct MR and model area measurements

Area (mm^2)					
Specimen	**Contact**	**Direct**	**Model**	**% Difference**	**Avg % Difference**
1	**RL**	43.369	49.182	13.4	14.5
	RS	89.947	103.900	15.5	
2	**RL**	100.162	58.295	41.8	32.9
	RS	55.863	69.258	24.0	
3	**RL**	124.845	110.771	11.3	7.5
	RS	63.410	65.768	3.7	

Table 3.4 shows the percent difference between experimental and model force measurements. For Specimens 2 and 3 percent differences in radiolunate contact force were relatively small (12.6 and 18.8% respectively). Percent differences in Specimen 1 radiolunate contact force and Specimen 3 radioscaphoid contact force were outside the validation criteria, but were plausible results. Percent differences in Specimens 1 and 2 radioscaphoid contact forces were unexpectedly high due to high and unreasonable model results. This led to high average percent differences for Specimens 1 and 2, and the percent difference for Specimen 3 fell just outside the validation criteria.

The fact that experimental results (Tekscan) closely matched direct contact area measurements was evident from average percent differences shown in Table 3.5. Aside from Specimen 1 radioscaphoid contact, all results were within 10%. The overall average percent difference was less than 10% for Specimens 2 and 3 (7.7 and 4.6% respectively) and just over 10% for Specimen 1 (11.6%).

Comparing Tekscan and model contact area measurements (Table 3.6), average percent differences closely matched for Specimens 1 and 3 (12.2 and 12% respectively). Comparing direct MR and model contact area measurements (Table 3.7), average percent differences also closely matched for Specimens 1 and 3 (14.5 and 7.5% respectively). For model results, due to underestimation of radiolunate contact area and a somewhat overestimation of radioscaphoid contact area, average percent differences in contact area measurements for Specimen 2 were nearly twice the level of the validation criteria.

Percent differences in peak contact pressure measurements between Tekscan and model varied from as low as 5.5% (Specimen 1 radioscaphoid contact) to as high as 80.4% (Specimen 3 radioscaphoid contact). Average percent differences closely matched for Specimen 2 (11.7%), but were high for Specimen 1 (42.1%) and Specimen 3 (66.2%).

3.4. Discussion and Conclusion

Overall behavior of the specimens was consistent and MRI-based models yielded results that were plausible in most cases. Prior studies have shown Tekscan sensor (11% accuracy) to be more reliable than Pressurex film (18% accuracy) [32]. This is evident from the Pressurex data acquired during this study. Due to this unreliability, Pressurex measurements were excluded from the validation criteria. Our data indicates contact area is the most consistent and reliable model measure, compared to Tekscan and direct MR measurements. This is a key parameter that would also be measurable from images in future *in vivo* studies. Contact force and especially peak contact pressure are highly dependant on geometric details and thus show higher variability.

Considering the validation criterion of contact area, the models for Specimens 1 and 3 were validated based on both Tekscan and direct MR measurements. The average percent difference for Specimen 2 did not fall within the 15% criteria, and this model was thus not validated for contact area. Accuracy in contact area did not necessarily insure accuracy in contact force or peak pressure, nor did contact area errors necessarily result in high force or peak pressure errors. This is evident from the average percent differences in peak contact area measurements. Specimen 2 did not meet the validation

criterion for area but had the best pressure match. The average percent difference fell well within the 25% criteria. This perhaps indicates the arbitrariness of the validation criteria levels. With occurrence of injury, changes in contact pressure distribution on the articular surface are to be expected. These changes can perhaps easily vary from 50% to as high as 100%. Based on this, it is difficult to set a definitive level of accuracy to make this a useful tool. The specified 25% error is probably not as good as the ideal that we would want to achieve (which is less than 10%). Considering the validation criterion of force, average percent difference in contact force for Specimen 3 was just outside the validation criterion. Specimen 3 radiolunate contact force fell within the 20% criteria while the radioscaphoid force error was over the criterion, but the value was plausible. The unexpectedly high model radioscaphoid contact force results for Specimens 1 and 2 resulted in high average percent differences. It should be taken into consideration that relative error may appear high, while absolute value for Specimen 2 is not implausible. However, the radioscaphoid force for Specimen 1 is nearly double the applied experimental force. Model contact area and peak pressure for this articulation are both accurate. Thus, it appears that geometric and/or kinematic errors led to overall higher pressures throughout the contact region, resulting in the error in force.

Considering experimental data, however, Pressurex results were unreliable, which could be attributed to nature of static and permanent pressure measurement. Due to inhomogeneity of joint fossa, artifacts could have influenced intensity profiles especially during insertion and removal of template. This Fuji-scale film error becomes

more prominent at low loads. Also, at high loads, intensity profiles near saturation, which lowers sensitivity and increases errors. Finally, the Fuji-scale film has a threshold for dye release. Any loads/pressures under the threshold will not be recorded. Tekscan sensor appeared to provide very consistent results. In order to better match articular contact fossa, sensor was trimmed and resealed to prevent fluid seepage from disrupting sensor readings. Due to presence of sensor in joint space articulations may have been somewhat altered due to sensor thickness and added stiffness [40]. Thickness and stiffness of film affects conformity between articulating surfaces and this could have impacted pressure measurements. This might have factored in the relatively high pressure readings obtained for Specimen 1 radiolunate contact and Specimen 3 radiolunate and radioscaphoid contacts. Very low percent error (less than 10%) between Tekscan and direct MR contact area measurements indicate this method to be a reliable standard for comparison when shifting to future *in vivo* analysis.

Results obtained from MRI-based models are comparable to results from similar radiocarpal contact analysis studies conducted in the past [31,32]. While refinements in image resolution and radiocarpal joint loading (loading five tendons as opposed to three to improve joint stability) have helped improved accuracy, the significant difference between this study and prior studies is the disparity in image resolution between unloaded and loaded MR images. Lower resolution loaded images may have reduced the accuracy of kinematic registrations. Due to the low resolution loaded images, bone geometry might not have been accurately isolated. Loaded image volume sets were also resized to properly perform registration. Prior validation studies have acquired both

unloaded *and* loaded images in similar high resolution [32]. The downside to higher resolution is longer scan time, which would not be feasible for active grasp. This would increase possibility of fatigue and motion artifacts in the images. On the other hand, there is not much impact of long scan times when acquiring images in the relaxed configuration. Keeping this in mind, loaded images were acquired at half the resolution of unloaded images for this study. This could provide a possible explanation for some of the inconsistent model results. Contact analysis was performed for a uniform cartilage thickness of 1 mm on each bone. Physiologically, cartilage thickness is non-uniform and varies with articulation across the surface of bones. Also, non-linear stiffness behavior of articular cartilage was not taken into consideration. Articular cartilage serves to distribute loads across joint surface thereby minimizing stress concentration and facilitating joint motion with minimal friction and wear. The elastic modulus of articular cartilage varies with rate of loading and can approach relatively high values with physiologic rates of dynamic loading. At slow loading rates, the effective elastic modulus is relatively low, but at high dynamic loading rates (running, for example) stiffness may approach 500 MPa [41]. Depending on application, these variations may produce different effects. At lower static loads, these effects may be secondary and not critical enough. Due to the low static loads (to simulate light grasp) implemented in this study, a low value of (linear) effective compressive modulus was assumed. In the published literature, articular cartilage is commonly assumed to be linear elastic for quasi-static loading or to consider only instantaneous response of the

tissue to loading [25-38]. This could further explain some of the inconsistent model results.

Several refinements in the modeling technique contributed to improvement of model accuracy for this study. Use of a custom coil and CISS sequence (compared to gradient recall echo sequence used in prior studies) improved quality of MR images. Bone contours and articular boundaries were better defined leading to improved isolated and segmented images. The greater number of slices constituting the image sets, resulted in more information from which to generate geometrically accurate models. For this study, unloaded images comprising individual volumes were scanned with 0.5 mm slice thickness. In prior studies, multiple image (1 mm thickness) sets were scanned at an offset and compiled to simulate 0.5 mm slice thickness. The prior procedure was found to be less accurate and sometimes resulted in different image contrasts that prevented consistent segmentation [32]. Another refinement for this study was quality control. For consistency, isolations and segmentations were reviewed by at least two individuals to minimize geometric errors from segmentation and errors in bone isolation for image registration. The second level review led to improved accuracy and consistency in contact analyses. Improvements were also made to the registration procedure used for kinematic analysis. Instead of relying on voxel registration as the standard [32], a combination of surface and voxel registration was used to obtain better kinematics. In addition, registration transformation selection was also secondarily reviewed.

One way to improve future accuracy would be to use patient specific cartilage measurements. This study used a uniform thickness of 1 mm based on literature. Instead, cartilage thickness could be measured from individual high resolution MR images and averaged to obtain a value. Another way would be to take into account variable cartilage thickness. Instead of specifying uniform articular surface thickness as a contact criterion, variable cartilage thickness models can be created for analysis. Further, the same input data could be implemented in a deformable contact FE model incorporated together with non-linear stiffness characteristics of articular cartilage.

While the method is clearly not perfect, it demonstrates excellent potential. Results show MRI-based models generated from 3 Tesla clinical MR scanner to be partially validated. Therefore, further development work is warranted, as well as preliminary work for the next phase with *in vivo* measurements in injured and normal joints.

3.5. References

1. Andriacchi TP, Mundermann A, Smith RL, Alexander EJ, Dyrby CO, Koo S. A Framework for the *in Vivo* Pathomechanics of Osteoarthritis at the Knee. Ann Biomed Eng 2004;32(3):447-57.
2. Fregly BJ, Bei Y, Sylvester ME. Experimental evaluation of an elastic foundation model to predict contact pressures in knee replacements. J Biomech 2003;36(11):1659-68.
3. Fregly BJ, Sawyer WG, Harman MK, Banks SA. Computational wear prediction of a total knee replacement from in vivo kinematics. J Biomech 2005;38(2):305-14.
4. Genda E, Horii E. Theoretical stress analysis in wrist joint--neutral position and functional position. J Hand Surg [Br] 2000;25(3):292-5.
5. Genda E, Konishi N, Hasegawa Y, Miura T. A computer simulation study of normal and abnormal hip joint contact pressure. Arch Orthop Trauma Surg 1995;114(4):202-6.
6. Manal K, Lu X, Nieuwenhuis MK, Helders PJ, Buchanan TS. Force transmission through the juvenile idiopathic arthritic wrist: a novel approach using a sliding rigid body spring model. J Biomech 2002;35(1):125-33.
7. Tsumura H, Miura H, Iwamoto Y. Three-dimensional pressure distribution of the human hip joint--comparison between normal hips and dysplastic hips. Fukuoka Igaku Zasshi 1998;89(4):109-18.
8. Woltring HJ. 3-D attitude representation of human joints: a standardization proposal. J Biomech 1994;27(12):1399-414.

9. Ahn HS, DiAngelo DJ. Biomechanical testing simulation of a cadaver spine specimen: development and evaluation study. Spine 2007;32(11):E330-6.
10. Anderson DD, Daniel TE. A contact-coupled finite element analysis of the radiocarpal joint. Semin Arthroplasty 1995;6(1):30-6.
11. Buchler P, Ramaniraka NA, Rakotomanana LR, Iannotti JP, Farron A. A finite element model of the shoulder: application to the comparison of normal and osteoarthritic joints. Clin Biomech (Bristol, Avon) 2002;17(9-10):630-9.
12. Gardiner JC, Weiss JA. Subject-specific finite element analysis of the human medial collateral ligament during valgus knee loading. J Orthop Res 2003;21(6):1098-106.
13. Li G, Gil J, Kanamori A, Woo SL. A validated three-dimensional computational model of a human knee joint. J Biomech Eng 1999;121(6):657-62.
14. Li Z, Alonso JE, Kim JE, Davidson JS, Etheridge BS, Eberhardt AW. Three dimensional finite element models of the human pubic symphysis with viscohyperelastic soft tissues. Ann Biomed Eng 2006;34(9):1452-62.
15. Mesfar W, Shirazi-Adl A. Biomechanics of the knee joint in flexion under various quadriceps forces. Knee 2005;12(6):424-34.
16. Penrose JM, Holt GM, Beaugonin M, Hose DR. Development of an accurate three-dimensional finite element knee model. Comput Methods Biomech Biomed Engin 2002;5(4):291-300.

17. Taddei F, Pancanti A, Viceconti M. An improved method for the automatic mapping of computed tomography numbers onto finite element models. Med Eng Phys 2004;26(1):61-9.
18. Anderson AE, Peters CL, Tuttle BD, Weiss JA. Subject-specific finite element model of the pelvis: development, validation and sensitivity studies. J Biomech Eng 2005;127(3):364-73.
19. Anderson DD, Deshpande BR, Daniel TE, Baratz ME. A three-dimensional finite element model of the radiocarpal joint: distal radius fracture step-off and stress transfer. Iowa Orthop J 2005;25:108-17.
20. Anderson DD, Goldsworthy JK, Li W, James Rudert M, Tochigi Y, Brown TD. Physical validation of a patient-specific contact finite element model of the ankle. J Biomech 2007;40(8):1662-9.
21. Beek M, Koolstra JH, van Ruijven LJ, van Eijden TM. Three-dimensional finite element analysis of the cartilaginous structures in the human temporomandibular joint. J Dent Res 2001;80(10):1913-8.
22. Carrigan SD, Whiteside RA, Pichora DR, Small CF. Development of a threedimensional finite element model for carpal load transmission in a static neutral posture. Ann Biomed Eng 2003;31(6):718-25.
23. Donahue TL, Hull ML, Rashid MM, Jacobs CR. A finite element model of the human knee joint for the study of tibio-femoral contact. J Biomech Eng 2002;124(3):273-80.

24. Koolstra JH, van Eijden TM. Combined finite-element and rigid-body analysis of human jaw joint dynamics. J Biomech 2005;38(12):2431-9.
25. Roarty CM, Grosland NM. Adaptive meshing technique applied to an orthopaedic finite element contact problem. Iowa Orthop J 2004;24:21-9.
26. Cheng HK, Lin C, Lin Y, Chen AC. Biomechanical evaluation of the modified double-plating fixation for the distal radius fracture. Clin Biomech 2007;22(5):510-7.
27. Troy KL, Grabiner MD. Off-axis loads cause failure of the distal radius at lower magnitudes than axial loads: a finite element analysis. J Biomech 2007;40(8):1670-5.
28. Ezquerro F, Jimenez S, Perez A, Prado M, de Diego G, Simon A. The influence of wire positioning upon the initial stability of scaphoid fractures fixed using Kirschner wires: a finite element study. Med Eng Phys 2007;29(6):652-60.
29. Kwak SD, Blankevoort L, Ateshian GA. A Mathematical Formulation for 3D Quasi-Static Multibody Models of Diarthrodial Joints. Comput Methods Biomech Biomed Engin 2000;3(1):41-64.
30. Pillai RR, Thoomukuntla B, Ateshian GA, Fischer KJ. MRI-based modeling for evaluation of in vivo contact mechanics in the human wrist during active light grasp. J Biomech 2007;40(12):2781-7.
31. Thoomukuntla BR, McIff TE, Ateshian GA, Bilgen M, Toby EB, *Fischer KJ*. Preliminary validation of MRI-based modeling for evaluation of joint mechanics. Journal of Musculoskeletal Research (*in press*).
32. Waller AJ. Master's Thesis: Refinement and validation of MRI-based models for joint contact mechanics. Mechanical Engineering, University of Kansas, 2007.

33. Anderson DD, Goldsworthy JK, Li W, Rudert MJ, Tochigi Y, Brown TD. Physical validation of a patient-specific contact finite element model of the ankle. J Biomech 2007;40(8):1662-9.
34. Song Y, Debski RE, Musahl V, Thomas M, Woo SL. A three-dimensional finite element model of the human anterior cruciate ligament: a computational analysis with experimental validation. J Biomech 2004;37(3):383-90.
35. Pfaeffle J, Blankenhorn B, Stabile K, Imbriglia J, Goitz R. Development and validation of a computed tomography-based methodology to measure carpal kinematics. J Biomech Eng 2005;127(3):541-8.
36. Shim VB, Pitto RP, Streicher RM, Hunter PJ, Anderson IA. Development and validation of patient-specific finite element models of the hemipelvis generated from a sparse CT data set. J Biomech Eng 2008;130(5):051010.
37. Papaioannou, G., et al., Patient-specific knee joint finite element model validation with high-accuracy kinematics from biplane dynamic Roentgen stereogrammetric analysis. J Biomech 2008;41(12):2633-8.
38. Anderson, A.E., et al., Validation of finite element predictions of cartilage contact pressure in the human hip joint. J Biomech Eng 2008;130(5):051008.
39. Kapandji A. Biomechanics of pronation and supination of the forearm. Hand Clin 2001;17(1):111-22.
40. Wu JZ, Herzog W, Epstein M. Effects of inserting a pressensor film into articular joints on the actual contact mechanics. J Biomech Eng 1998;120(5):655-9.
41. Skeletal Tissue Mechanics. R. Bruce Martin. Springer, New York. 1998.

4. Summary and Future Direction

Results obtained from both the effect of film and validation studies illustrated the strengths and weaknesses of the MRI-based modeling approach. The model results for contact area were validated for 2 of 3 specimens and peak pressure was validated for one specimen. These partial validation results further demonstrate the need for development and additional application of MRI-based models for study of radiocarpal contact mechanics. Each study is summarized in more detail below, along with recommendations for future endeavors in this area.

The effect of inserting a sensor into radiocarpal joint space on kinematics and contact characteristics was investigated. The presence of film clearly alters the result, but the effects do not appear completely predictable. A single cadaver forearm specimen was used and analyzed for simulated light grasp (110 N loading of tendons). Models were constructed from MR scans obtained using a 9.4 Tesla scanner for unloaded and loaded configurations with and without Pressurex film inserted in joint space. Kinematics defining transformations from unloaded to loaded (with and without film) state were obtained and models adjusted to reflect presence of film in joint space. These were input in a contact modeling program for analysis. Contact characteristics (contact forces, areas and peak pressures) were then compared with and without the presence of film in the joint space. Kinematics were observed to be higher with film for translations and lunate rotation. The average percent difference in radiolunate and radioscaphoid contact areas was found to be higher with presence of film and comparable to other effect of film studies. Contact area was increased for both articulations, though the level of increase

varied. Also, the *average* percent difference in radiolunate and radioscaphoid peak contact pressures was found to be higher with the presence of film and close to the range reported by other studies. With the presence of film, radiolunate and radioscaphoid contact forces were overestimated and underestimated respectively. The presence of film clearly alters the contact. Thus, this may account for additional differences (beyond measure accuracy) between experimental and modeling measures.

When using sensors for *in vitro* experimental measurements, impact on kinematics and contact characteristics must be taken into consideration. To minimize errors, sensors with least geometric and stiffness parameters must be selected. Future testing of multiple specimens should be conducted to establish significant differences in kinematics and contact characteristics resulting from insertion of film in radiocarpal joint space.

Three cadaver forearm specimens were tested to validate MRI-based modeling with a clinical MR scanner for future *in vivo* studies. Dissections were performed to expose the radiocarpal joint for sensor insertion and to isolate the necessary tendons for joint loading. The two extrinsic wrist extensors and three extrinsic digital flexors were loaded with a total load of 110 N to simulate light grasp. Along with experimental joint contact measurements using Fuji-scale film and an electronic sensor, MR scans were taken in a 3 Tesla clinical scanner for both loaded and unloaded configurations. Models were created for the radius and two carpal bones (lunate and scaphoid) and kinematics defining transformations from the unloaded to loaded state were obtained. These were input in a contact modeling program for contact analysis. Contact characteristics (contact forces, areas and peak pressures) were then compared with experimental and direct measures.

Results obtained from this study were comparable to radiocarpal contact validation studies conducted in the past. Results showed models to be partially validated based on contact areas and peak pressures, but contact force data did not meet validation criteria. Peak contact pressure and force measurements were more variable than contact area data. Also direct measurement of contact area from MR images were found to be very close to experimental measurements showing this to be an appropriate validation method for future *in vivo* studies.

The main concern with models constructed from MR scans is the quality of the images. In order create accurate geometric models, images should have high resolution and signal to noise ratio. Image resolution also effects registration and kinematic analysis. The validation study protocols were based on protocols for future *in vivo* studies. Hence loaded images were acquired at half the resolution of unloaded images to minimize grasp scan time. Thus, resolution of loaded images could have led to errors in kinematics explaining some of the discrepancies between contact model and experimental measurements.

The approach can be augmented in several ways. Patient specific average cartilage thickness or variable cartilage thickness models can be used to improve contact accuracy. Instead of contact models, FE models can be used to obtain more accurate and in depth results characterizing stresses and strains during functional joint loading.

While the method is clearly not perfect, it demonstrates excellent potential. Results show MRI-based models generated from 3 Tesla clinical MR scanner to be partially

validated and therefore further development and initiation of the next phase with *in vivo* measurements is warranted.

In vivo contact mechanics data can provide a means to determine the effects of injury and the efficacy of surgical procedures used to treat joint injuries. MRI-based contact modeling can be used to investigate injuries such as unilateral scapholunate dissociation and unilateral distal radius fracture and corresponding surgical interventions (such as proximal row carpectomy, scapholunate ligament repair and fusions). Without the presence of implants, changes in joint mechanics can be identified between 1) normal and injured wrist, 2) injury and surgical reconstruction or 3) normal wrist and surgical reconstruction.

Changes in joint mechanics following injury and reconstruction can be monitored, and these changes can be related to the risk of OA over time. Long-term data acquired from injured human subjects, observed for a period of time to monitor for progressive joint degeneration, may identify key factors leading to DJD/OA. It may be possible to identify which of these injuries indicate OA risk due to altered joint mechanics and predict who is at high risk to develop OA.

The focus of our research to this point has been the radiocarpal joint. OA is not restricted to the wrist, but also affects other joints as well with varying degrees of severity. In terms of incidence, the knee is the most common joint affected by OA. The scope of MRI-based modeling can be expanded to include *in vivo* joint contact mechanics of the knee (patellofemoral joint mechanics, for example), along with other complex joints such as the ankle, to predict OA risk.